Enhanced protein crystallization on Nafion® membranes modified by low-cost surface patterning techniques

M. Polino [1], C. A. M. Portugal [1], H. Le The [2], R. Tiggelaar [3], J. Eijkel [2], J. G. Crespo [1], I. M. Coelhoso [1], M. P. Pina [4,5]*, R. Mallada [4,5]*

[1] LAQV-REQUIMTE/CQFB, Department of Chemistry, FCT/Universidade Nova de Lisboa, Portugal

[2] BIOS Lab-on-a-Chip, MESA+ Institute for Nanotechnology, University of Twente, The Netherlands

[3] NanoLab Cleanroom, MESA+ Institute for Nanotechnology, University of Twente, The Netherlands

[4] Nanoscience Institute of Aragon (INA), Instituto de Ciencia de Materiales de Aragon (ICMA), Department of Chemical and Environmental Engineering, Universidad de Zaragoza, Spain

[5] Instituto de Ciencia de Materiales de Aragon (ICMA), Universidad de Zaragoza-CSIC, Zaragoza, Spain

*Corresponding authors: imrc@fct.unl.pt, mapina@unizar.es

Keywords: Nafion membrane; soft lithography; surface topography; interfacial interactions; crystallization

Abstract

In this work, the influence of surface topography on protein crystallization over Nafion® is investigated. Two types of Nafion® based membranes were modified by soft lithographic techniques in order to create different topographies at the micro and nano scale and subsequently tested. From the analysis of the induction time, nucleation and crystal growth rate of Trypsin from Bovine Pancreas, all the patterned Nafion® based membranes show an enhanced nucleation and crystal growth. To provide additional insight to the experimental observations, the wettability properties of the prepared samples and the ratio of the Gibbs free energy of heterogeneous nucleation to homogeneous nucleation were evaluated. The crystallization outcome results from the combined effect of both, the structural and chemical properties of the nucleant Nafion® surface.

Introduction

X-ray crystallography is the main technique used for solving the tri-dimensional structure of proteins. The main limitation of X-rays analysis is the attainment of well-diffracting crystals of biological macromolecules [1,2]. The key event for obtaining protein crystals suitable for

x-ray diffraction is nucleation. Nucleation is a phase change, occurring in supersaturated solutions that reinstate equilibrium by clustering protein molecules in small solid nuclei. This leads to the formation of an interface between the solid nuclei and the solution creating the need for overcoming an activation energy for the process to occur. In other words, nucleation only becomes effective when the nuclei reach a critical size [3,4]. It is well known that the interaction of the target solution with external substrates, also denominated as nucleant surfaces, alters the Gibbs free energy of the nucleation process promoting or inhibiting nucleation (heterogeneous nucleation) [5]. Heterogeneous nucleation for protein crystals was first reported in 1988, by McPherson, growing protein crystals onto minerals with a similar crystalline lattice (epitaxy) [6]. From there on, several nucleant surfaces were investigated and several chemical interactions between protein molecules and surfaces were hypothesized as effective control mechanisms: ionic interactions, hydrogen bonding and hydrophobic interactions [7–11]. Furthermore, an always increasing number of studies are pointing out how combining chemical interactions with a suitable surface topography at the nanoscale might enhance the probability of nucleation. For instance, Shah et al. [12–15] noticed the preferential nucleation of proteins in the pores of nucleant particles, i.e. ordered mesoporous silica with 4-20 nm average pore size, for a given relationship between the protein radius of gyration and specific pore diameter of the nucleant particle. They also hypothesised a further stabilization of the nuclei formed in the nucleant pores induced by the presence of specific chemical moieties (such as –OH, -NH_3 or CH_3) on the pore wall [14,15]. Ghatak et al. [16,17], obtained protein crystals without the help of precipitant by combining a wrinkled PDMS surface with an oxidation treatment. Recent efforts are oriented towards the evaluation of topography and roughness effect on nucleation over nucleant surfaces without altering its surface chemistry. According to the literature review, the creation of different topographies at the nanoscale is mainly associated with local changes in the surface chemistry, i.e. induced by plasma or wet oxidation treatments, or specific coatings. Thus, Liu et al. [18] investigated the performance of chemically modified glass slides with different polymers on the heterogenous nucleation of lysozyme crystals. They found that both, the surface chemistry (by controlling the chemical and physical interactions with the protein molecules), and the surface topography (by increasing the possibility of nucleation compared with that on an ideally flat surface) of the modified glass slide affect the heterogeneous nucleation to different extents. Recently, a similar study has

been reported for several model proteins on muscovite mica substrates modified with multilayers of 1,3,5-tris(10-carboxydecyloxy) benzene (TCDB) grown by evaporation. The surface roughness (up to 3 nm) and wettability properties were correlated with the amount of TCDB deposited [19] and with the protein crystallization outcome. Topography effects were also investigated by modifying the surface of conventional protein crystallization plates with various types of wet oxidation treatments [20] in order to generate different degrees of roughness (up to 32 nm).

During the last twenty years, membranes have been used in crystallization processes to control solvent transport and hence the supersaturation rate; and also as heterogeneous nucleation promoters by inducing a reduction in the free energy barrier [21]. Indeed, the physical properties, i.e. porous structure, and chemical nature of the membrane surface control the mass transfer rate of components and provide at the same time the micro-nano environment for crystal nucleation and growth [22–25]. The use of microporous hydrophobic supports covered with an hydrophilic hydrogel layer allows the production of protein crystals with improved diffraction properties due to the convection-free environment of the gel [26]. Recently, the tuning of chemical and topographical features of similar hydrogel composite membranes by incorporating different amounts of iron oxide nanoparticles [27] has been investigated for model proteins crystallization by our group. As the NPs were introduced in the hydrogel composite membrane, the crystal density number increased with the increase of the NPs load.

The fabrication of nucleant surfaces with a tunable topography whereas preserving the chemical nature of the pristine material seems to be a priority for a more comprehensive understanding of the nucleation mechanisms. To the best of our knowledge, there are no previous works where the influence of nucleant topography is systematically investigated keeping unaltered the chemical composition of the surface. Nowadays, soft lithography outstands as a convenient, effective, and low-cost method for the formation and manufacturing of micro- and nanostructures. It includes a set of techniques that make use of an elastomeric stamp, namely a PDMS stamp, to generate patterns and structures with feature sizes ranging from 30 nm to 100 μm. Thus, it is possible to design tailored geometries at different scales and transfer them to different surfaces minimizing surface chemistry changes. This approach is cleanroom free and high-throughput process, which

makes micro and nano-fabrication affordable for a wide range of applications. Basically, it relies on the fabrication of a silicon master mold that is further used to prepare the PDMS elastomeric stamp or mold by casting. The PDMS replicas can be then used repeatedly for thermal nanoimprint lithography or microtransfer molding processes [28]. More specifically, thermal nanoimprint lithography (NIL) is a powerful and inexpensive technique for reproducing large patterns onto thermoplastic materials [29–31]. It takes advantage of the ability of materials to become soft and suffer deformation at temperatures higher than their glass transition temperature (Tg) and reinstate their stiffness at temperatures below the Tg. In microtransfer molding (MT) and replica molding (REM), a liquid prepolymer is poured onto the patterned surface of the PDMS mold. In REM, this mold is overloaded with the prepolymer solution; and then, is cured to a solid by illuminating the mold with UV light or by heating it. When the PDMS mold is peeled away carefully, a patterned microstructure is left on the surface of the substrate. In MT approach, the removal of the prepolymer excess poured on the PDMS mold is carefully performed before curing.

This work explores the use of soft lithographic techniques for the micro and nanopatterning of Nafion® based membranes. This type of ion-exchange membranes has been selected due to its protein crystal derivatization performance, recently demonstrated by our group [32]. Hence, optimizing a membrane surface suitable for a gentle derivatization, besides a more controlled nucleation, would allow for creating a nucleant support suitable for all steps required for protein X-ray resolution.

In particular, three different fabrication approaches are herein investigated: i) thermal NIL for the micro and nanopatterning of commercial Nafion® 117 flat membranes using hard molds; ii) MT and REM to pattern microstructures upon thermal curing of the Nafion™ NR50 superacid resin solution spread on the PDMS mold; and iii) the combination of both to obtain a hierarchical structure by hot pressure assembly of single micropatterned (MT) and nanopatterned (NIL) membranes, respectively. The crystallization performance of all the prepared membranes, i.e. induction time, nucleation and growth rate, is evaluated using Trypsin from Bovine Pancreas as protein model and compared to the crystallization on Nafion® 117 flat membrane. Although further investigation with other proteins would be required to extend the knowledge gathered in this work, the obtained results with Trypsin protein are relevant enough due to the fact that it is widely used in various biotechnological

processes and food processing [33] and it presents structural similarities with other types of proteolytic enzymes, for example viral proteases involved in the production of viral proteins that inhibit the host immune response and proteases involved in stress signalling, disfunction of which may lead to cancer or Alzheimer disease [34,35]. Finally, the effect of surface properties on protein crystallization is discussed on the basis of the classical nucleation theory by adapting the model developed by Liu et al. [18] to the designed geometries.

Materials and Methods

Flat Nafion® Membranes

Two types of flat Nafion® membranes are studied in this work: commercially available flat Nafion® 117 membranes (average equivalent weight 1100 g per sulfonic group and 178 µm thickness) purchased from Sigma Aldrich; and those prepared from Nafion™ NR50 superacid resin purchased from Ion-Power in the form of beads. Flat Nafion™ NR50 based membranes were obtained by casting on a Petri dish from a diluted solution in N,N-Dimethylformamide (DMF). According to the technical specifications of the suppliers, both Nafion materials possess the same equivalent weight (1100 g/eq). However, the resulting flat membranes exhibit different macroscopic properties, i.e. water uptake: i.e. 15% wt. for Nafion™ NR50 vs. 24% wt. for Nafion® 117, which may be attributed to the membrane formation process. The influence of solvent on the Nafion molecular conformation in dilute solutions is well reported in the literature [36], and thus the morphology and macroscopic properties of the resulting membranes are greatly affected.

Hard molds for Thermal Nanoimprint Lithography (NIL)

Different topographies, with micro or nano features, were created on the surface of commercial Nafion® 117 membranes by thermal nanoimprint lithography. In particular, two rigid silicon molds were used. The nanomold used for the Nafion 117 nanopatterning was produced by displacement Talbot lithography [37]. This nanomold contains Au/Ti on cone-

shaped silicon features 110.7±2 nm in diameter and 115.4±0.5 nm in height with a pitch of 250 nm. The cone-shaped features are displayed in Figure 1.A and Figure 1.B before and after the residual resist removal on the top of the pillars (marked with a black line ~ 18 nm), respectively. All the 117 Nano membranes prepared in this work were imprinted with the mold containing the residual resist coating.

(A) (B)

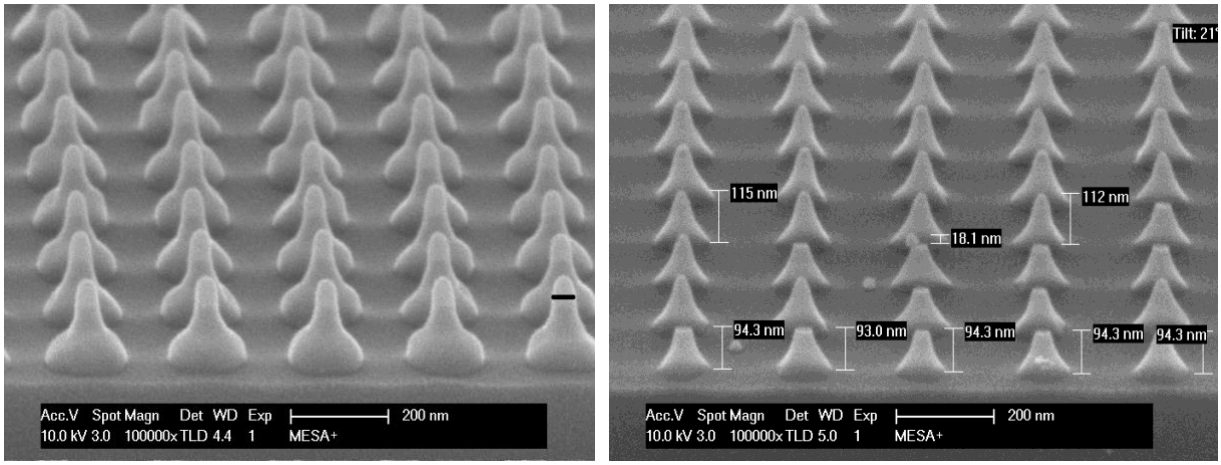

Figure 1. SEM images of the fabricated nanomold before (A) and after (B) residual resist removal.

The SU8 photoresist type micromold, not shown here, used for Nafion® 117 micropatterning was produced by standard photolithography (details are reported in the Supporting Information). It contains triangular shaped pillars with a side of 165±5μm and 152.5±7.5μm in height with a repeating unit of 182 μm x 347 μm.

Soft mold for Microtransfer Molding (MT) or Replica Molding (REM)

A similar microscale patterning was transferred to Nafion ™ NR50 by casting and curing the Nafion:DMF solution onto the poly(dimethylsiloxane) (PDMS) micromold (shown in Figure 2B). This elastomeric mold, with triangular-prism shaped pillars 160 μm side and 110 μm height and periodically ordered on the surface with a repeating unit of 347 μm x 182 μm, was produced by casting a mixture of PDMS pre-polymer (purchased by Sylgard 184 Dow Corning, Midland, MI) and curing agent (10:1) onto a SU8-Si master (shown in Figure 2A) fabricated by standard photolithography [38]. The PDMS solution casted onto the SU8-Si

master was cured by baking at 80°C for 50 minutes and the final elastomeric mold was released by peeling-off.

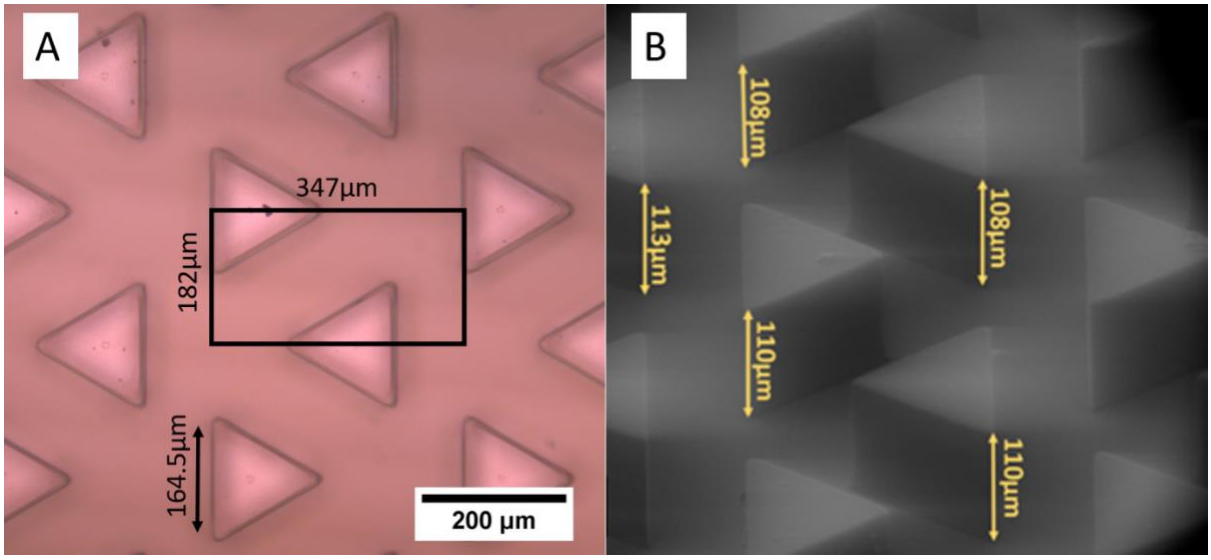

Figure 2. SEM images of the SU8-Si micromold (A) and PDMS micromold (B) used to prepare patterned Nafion membranes by NIL and MT respectively.

Patterning of Nafion® based membranes

Three different approaches are herein investigated to prepare 117 Micro, 117 Nano and NR50 Micro Nafion® based membranes (see Figure 3). All of them take advantage of the intimate contact of the Nafion substrate with a mold for transferring the designed structure.

The first approach is based on thermal NIL to prepare 117 Micro (when using the hard micro mold) and 117 Nano (when using the hard nano mold) samples, respectively. More specifically, Nafion® 117 flat membranes 178 µm thick were patterned using a Compact NanoImprint (CNI) tool from NILT company. Both, the Nafion® 117 substrate and the mold were contacted on the top of a ceramic heating plate. The chamber was closed and a program was set in order to firstly rise the temperature to 135°C to soften the membrane, 20°C above the glass transition temperature Tg of Nafion® 117 (referred to Supporting Information for its experimental determination from DSC analyses). Then, a pressure of 6 bar was applied for 6 minutes to improve the contact between the mold and Nafion® 117. Finally, the chamber was cooled down to 60 °C (to freeze the structure of the mold in the substrate) and the pressure released (see schematics in Figure 3A).

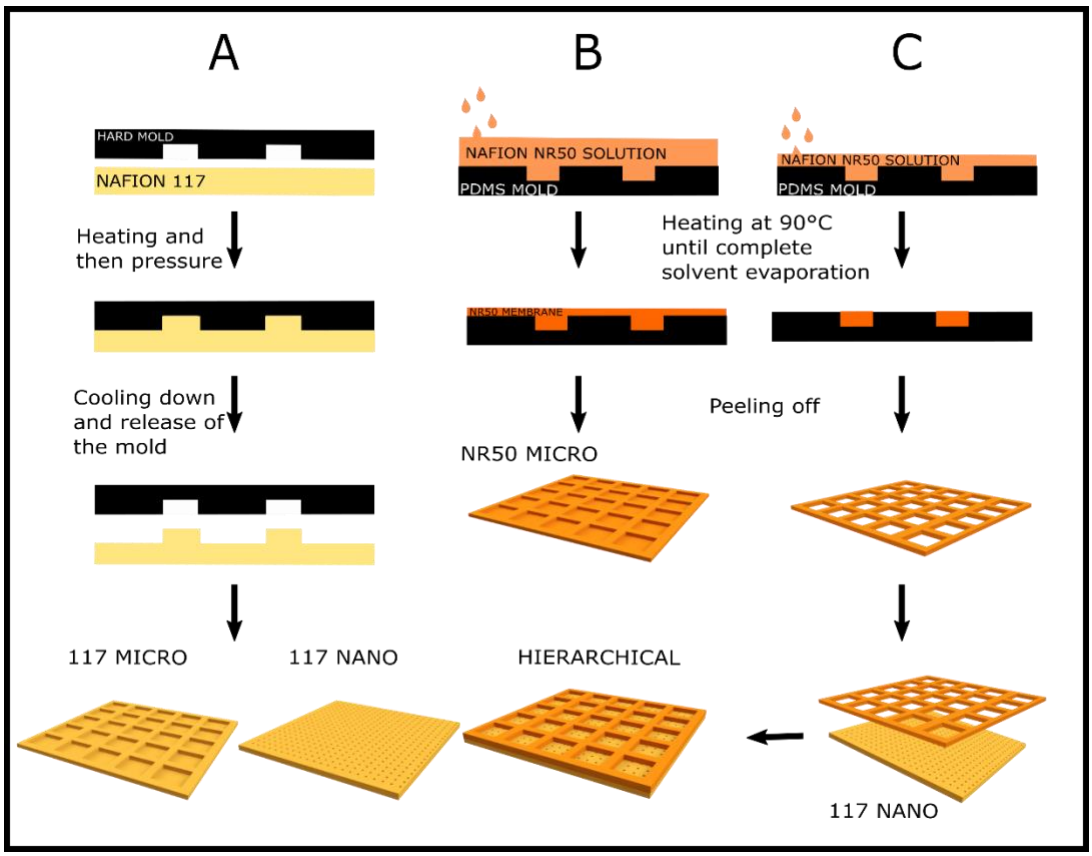

Figure 3. Schematics of the fabrication processes for patterned Nafion® membranes: A) thermal nanoimprint lithography (NIL) on Nafion 117 flat films to prepare 117 Micro and 117 Nano samples; B) replica molding (REM) to prepare NR50 Micro sample; and C) microtransfer molding (MT) to prepare Hierarchical sample by hot pressure assembly with 117 Nano.

The second strategy relies on REM and leads to NR50 Micro sample. Unlike previously, Nafion ™ NR50 beads were, instead, dissolved in N,N-Dimethylformamide (DMF) purchased from Acros, at 240°C for 24h in autoclave, at a concentration of 0.030g/mL (3.2% wt). The Nafion ™ solution was casted onto the PDMS mold and left on a hot plate at 90°C until complete evaporation of the solvent (see schematics in Figure 3B). Controlling the amount of polymer solution used for casting allows to tune the thickness of the Nafion substrate. When the thickness of the membrane is less than the height of the pillars (110±2µm), a NR50 Micro membrane with straight pores connecting both sides is obtained (See Figure 3C). In order to facilitate the release of the membrane, before Nafion ™ NR50 solution casting, the PDMS mold was treated with Tridecafluoro-1,1,2,2-tetrahydrooctyl-1-trichlorosilane (TFOCS, from Sigma Aldrich). Few drops of TFOCS were left evaporating and

deposited as a thin layer onto the PDMS mold to make it more hydrophobic [28]. All the NR50 based membranes were carefully washed in boiling water to remove traces of DMF solvent.

In the third strategy, a hierarchical structure with the nanowells inside the microwells is obtained by hot pressure assembly of NR-50 Micro (MT) and 117 Nano (NIL) membranes, respectively (see schematics in Figure 3C). The final hierarchical membrane combines the microstructured Nafion^{TM} NR50 membrane (90 μm thick) with straight pores connecting both sides and the nano imprinted Nafion® 117 membrane (178 μm thick).

Characterization Techniques

In order to evaluate the fidelity of master duplication in soft lithography techniques, the molds and the obtained Nafion® membranes were characterized by AFM (Multimode 8 from Veeco/Bruker), SEM (Inspect F50, FEI) and optical microscopy (Nikon Eclipse ci). Samples for SEM were sputtered either with Au/Pd or carbon. AFM images were processed by Gwyddion software[39] and SEM and optical microscopy images by Image J [40]. In order to track chemical changes that may occur during the imprinting process FTIR (Perkin Elemer, Spectrum Two, FT-IR Spectrometer) spectra, XPS analysis (Axis Ultra DLD (Kratos Tech.) equipment and exciting by the monochromatized AlKα source (1486.6 eV) at 15 kV and 10 mA) and ^{19}F NMR (Bruker 400WB Spectrometer) of the membranes were performed. The wetting properties of the patterned Nafion based membranes were studied based on the static contact angle (SCA) measurements. These were evaluated by the sessile drop method in a contact angle goniometer (CAM 100, KSV Instruments Ltd., Finland). The solution used for the measurement was the same solution used for the crystallization experiments, hence: Trypsin from Bovine Pancreas 20 mg/mL, Hepes buffer 12.5 mM (pH=7.5), $CaCl_2$ 5mM, Benzamidine 5mg/mL, $(NH_4)_2SO_4$ 0.1M, PEG 8K 10%, Cacodylate 0.05M (pH=6.5). Five independent measurements were performed on each sample to calculate the average value and standard deviation (SD). The drop volume used for the measurements was 9 μL.

Crystallization solutions

A solution of Trypsin from Bovine Pancreas (BPT), purchased from Panreac, with initial concentration of 40 mg/mL was prepared in 25mM Hepes buffer (pH=7.5), with 10mM $CaCl_2$ and 10mg/mL Benzamidine (in order to inhibit the protease activity). The precipitant solution, also used as stripping solution, was composed of $(NH_4)_2SO_4$ (purchased from Panreac) 0.2M, PEG 8K 20% wt (purchased from Sigma-Aldrich), and 0.1M of Cacodylate (purchased from Sigma Aldrich) pH=6.5. The final crystallization solution, after mixing the protein and precipitant solutions, was 20 mg/mL.

Crystallization experiments

Crystallization tests were carried out by using 24-well plates (from Qiagen) conventionally used for the vapor diffusion technique [1] and adapted for membrane-assisted crystallization experiments (sitting drop mode). The setup is displayed in Figure 4. Briefly, an equal amount (5 µL) of protein and precipitant solution was mixed on the top of the nucleant membrane (0.7 cm x 0.7 cm) and left equilibrating with 500 µL of stripping solution. The difference in water activity between the crystallization solution and the stripping solution determines solvent migration from the protein solution to the stripping solution, increasing protein concentration until supersaturation is reached promoting nucleation. The crystallization tests were carried out at 20 °C with five replicates for each condition to assure the results reproducibility. Crystallization trials were also carried out using flat Nafion membranes for reference purposes. Data over time, on nucleation and crystal growth, were obtained by monitoring the number of crystals and size with an optical microscope (Nikon Eclipse ci) equipped with a camera and pictures were processed with the ImageJ software [40].

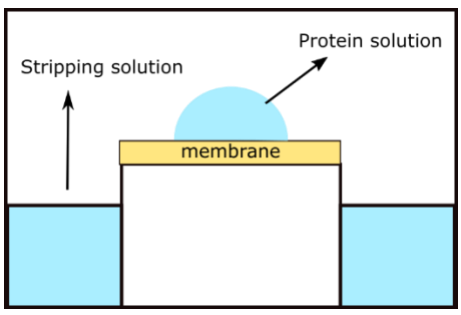

Figure 4. Experimental set-up used for crystallization experiments in vapour diffusion mode.

Results and Discussion

Characterization of the patterned topographies on Nafion® membranes

Figure 5 shows the top view of the 117 Nano and 117 Micro samples prepared by thermal NIL. For the nanostructured membrane (Figure 5A), SEM images reveal a repeating unit of 230 nm x 230 nm with cilindrical-shaped wells 110 nm diameter. Thus, the nanostructures on Nafion 117 replicate almost the inverse pattern of the master with periods smaller than the original of the rigid master due to large thermal expansion coefficient of thermoplastic Nafion ($200 \cdot 10^{-6}$ K^{-1})[41].

For the microstructured membrane (Figure 5B), optical microscope images indicate triangular-shaped wells 164 µm size and a repeating unit of 187 µm x 355 µm. Also in this case, the microstructure on the Nafion® 117 replicates closely the inverse pattern of the master.

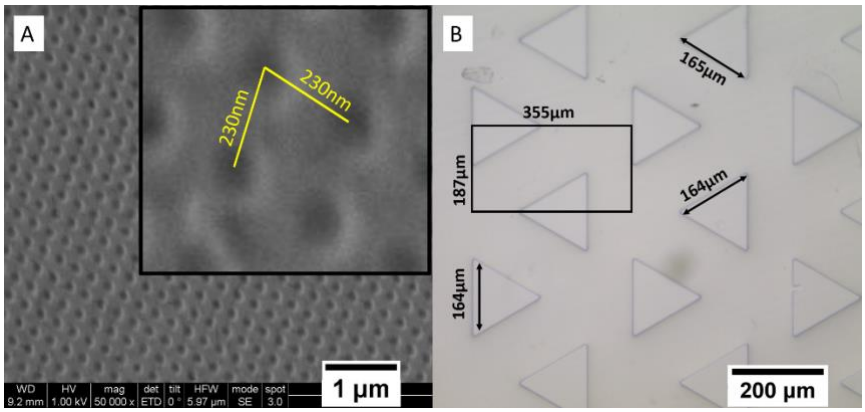

Figure 5. Top view images of: A) 117 Nano (SEM) and, B) 117 Micro (optical).

In addition, the imprint depth of the nanofeatures was analysed from 3D AFM images (see Figure 6) the depth of the wells was 56 ± 4 nm compared to the rigid master depth, 115.4±0.5 nm.

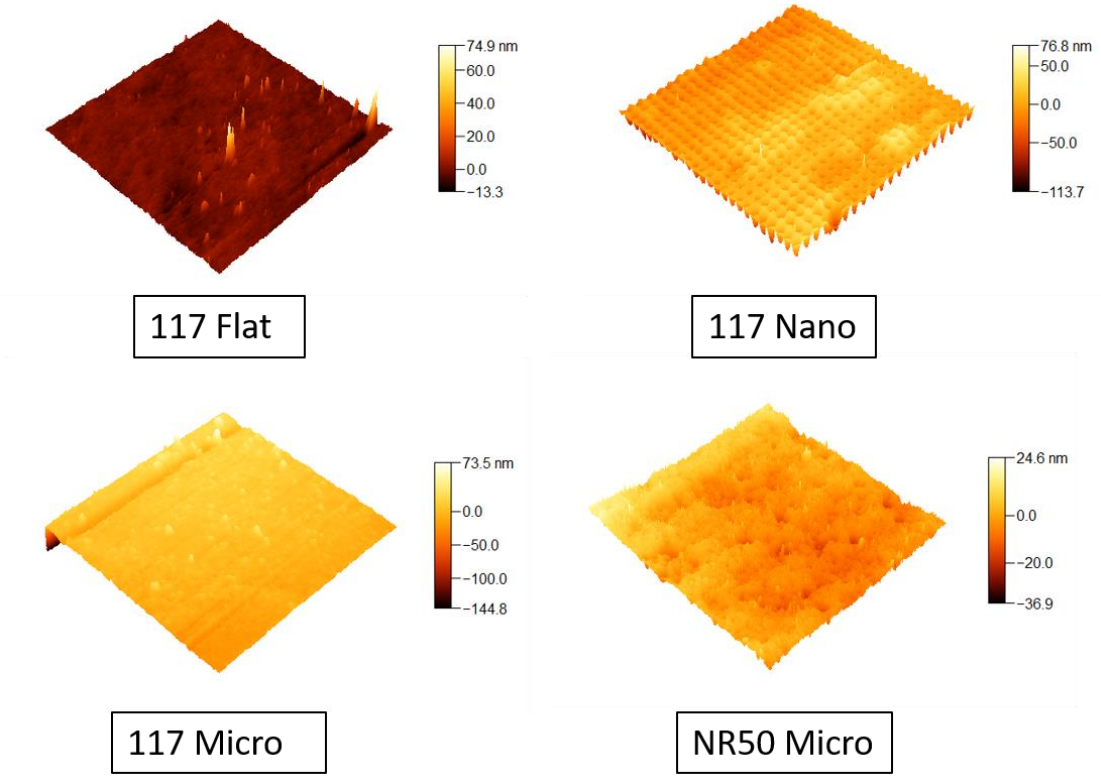

Figure 6. AFM images of the Nafion based membranes developed for this work. The scanned area was 5µmx5µm for all the membranes.

The AFM scanning was performed over the areas depicted in Figure 7. The processing of AFM images from the patterned surfaces by software Gwyddion [31] provides with the roughness parameters shown in Table 1: Ra (average of absolute values of profile height deviations from the mean line) and Rms (root mean square average of the profile height deviations from mean line).

Table 1. Main characteristics of the Nafion® based membranes studied in this work

Name	Starting Material	Patterning	Thickness (µm)	Ra [(1)] (nm)	Rms [(2)] (nm)	SCA (°)
117 Flat	Nafion® 117	n.a.	178	1.0±0.2	3.1±3.4	64.7±2.9
117 Nano	Nafion® 117	nano (NIL)	178	14.9±4.9	6.4±1.1	63.2±2.4
117 Micro	Nafion® 117	micro (NIL)	178	4.0±0.4	16.8±7.2	48.1±4.2
NR50 Flat	Nafion™ NR50	n.a.	90	n.a.	n.a.	77.7±4.4
NR50 Micro	Nafion™ NR50	micro (REM)	90	2.8±0.4	3.8±0.6	100.0±4.0
Hierarchical	Nafion® 117 + Nafion™ NR50	nano+micro (NIL+MT)	268	n.a.	n.a.	87.3±1.6

[(1)] Average Roughness; [(2)] Root-Mean-Square Roughness;

Herein, it is worthy to point out that the scanned line for determining the roughness on sample 117 Nano (as shown in Figure 7B) was drawn across the hillocks. Consequently, the surface roughness reported in Table 1 for 117 Nano is somehow overestimated when compared with its counterparts due to the periodic nanoholes are included in the averaging. In general, all the Nafion® based membranes show a rather smooth surface with comparable roughness at nanoscopic scale. As an example, 117 Flat and 117 Micro membranes, with clearly different topographies at a microscopic level, exhibit similar Ra values, i.e. 1.0±0.2 nm and 4.0±0.4 nm, respectively. In addition, whatever the soft lithography approach to obtain the desired microstructure, the surface roughness is comparable: 2.8±0.4 nm for NR50 Micro (REM) vs. 4.0±0.4 nm for 117 Micro (NIL).

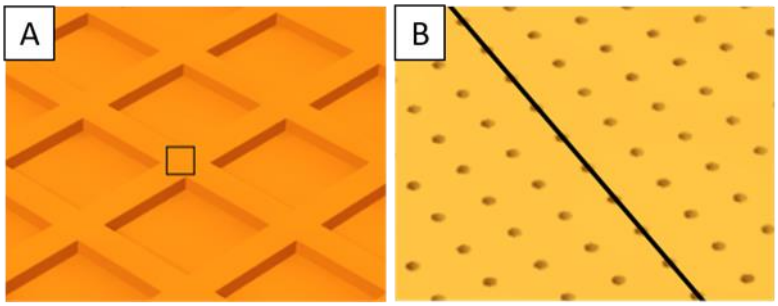

Figure 7. Scanned areas of patterned Nafion ® based membranes by AFM: A) analysis performed on the contour surface (black square) for117 Micro and not inside the wells); B) analysis performed on the black line for 117 Nano);

Influence of surface patterning on the wetting properties

Previous investigation was carried out to examine the potential influence of the imprinting temperature, 135ºC, on the surface chemistry and consequently on the surface wettability of samples processed by NIL. It has been reported that thermal treatment of Nafion® membranes may induce conformational changes and spatial reorientation of the hydrophobic an hydrophilic nanodomains leading to a lower water uptake and conductivity [42,43]. According to the literature, the thermal NIL herein performed would induce minor changes in water content (~2%) and negligible variations in its crystallinity [42]. In order to confirm such hypotheses, comparative XPS analyses were carried out for as received commercial Nafion® 117 membranes, i.e. sample Flat 117, and for thermal imprinted membranes, i.e. sample 117 Nano. Figure 8.a displays the C1s core level spectra of the two samples. According to literature [41], the peak centered at 282.7 eV is assigned to graphitic carbon atoms; and the peak at 289.8 eV is interpreted as the superposition of the signals

from –OCF–, $–OCF_2–$, $–CF_2–$ and $–CF_3$ groups. The recorded intensity for both peaks is rather similar on the reference 117 Flat sample. However, C1s spectrum for the thermally imprinted sample, 117 Nano, exhibits a higher contribution on the membrane surface of both: the $-CF_2–$ the hydrophobic domains, and of –OCF-, the hydrophilic domains, over graphitic carbon. This observation reinforces the adequacy of the thermal imprinting parameters but highlights the arrangement of the polymer chain conformation capable to modify the surface wetting properties of thermal NIL processed samples. The FTIR spectra (see supporting information Figure S2) are almost overlapping with the exception of the band centered at 3451 cm^{-1}, attributed to the stretching of –OH group and only slightly more intense for 117 Flat (reference) sample. When comparing 19F NMR spectra (see supporting information), all the Nafion based samples resemble identical.

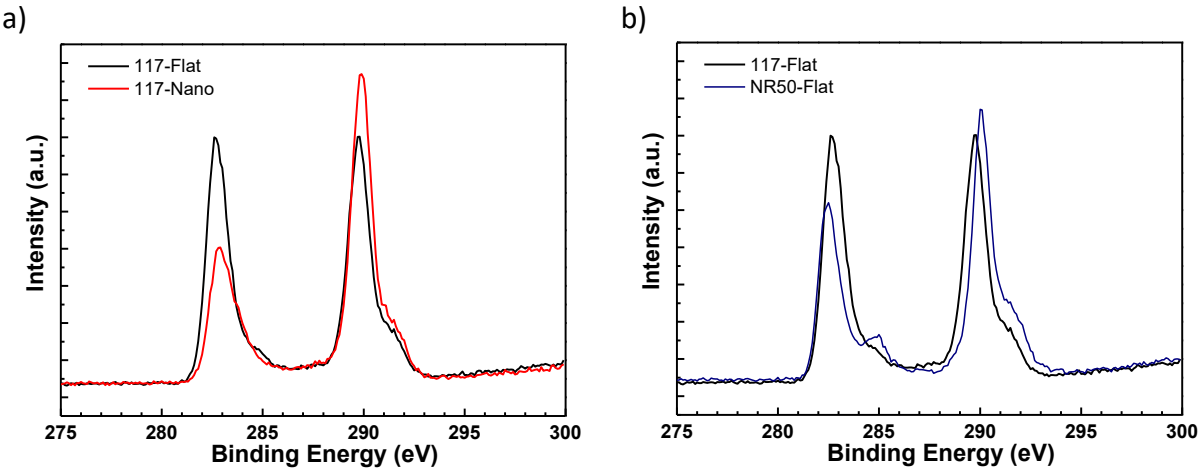

Figure 8. Comparative XPS analyses of Nafion based membranes: a) commercial 117 Flat (reference) and patterned 117 Nano (NIL);b) as received 117 and casted NR50 Flat membranes.

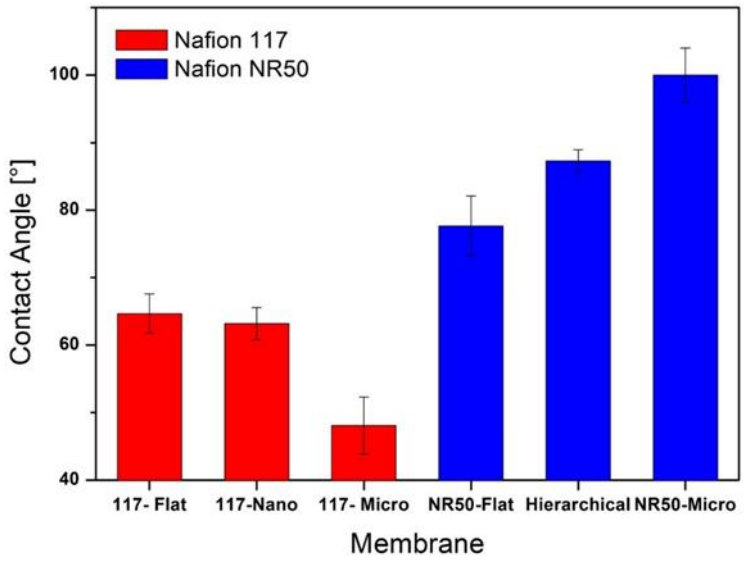

Figure 9. Comparison of SCA values for all the Nafion ® based membranes studied in this work.

The determination of the static contact angle, SCA, allowed the establishment of the membranes` wettability. The experimental measurements were performed using the same protein solution as the one used for crystallization experiments. The patterning effect on wetting properties is shown in Figure 9 for the two Nafion based materials. An apparent opposite behaviour is shown by Nafion® 117 and Nafion™ NR50 samples, respectively. As an example, the SCA registered for 117 Micro and NR50 Micro samples with common features on the surface, are 48±4.2° and 100±4° respectively. Although both starting materials exhibit the same equivalent weight (1100 g/eq) and ion-exchange capacity (0.9meq/g) [36]; the membrane formation process greatly influences the arrangement of the polymer chain conformation and mobility, leading to noticeable variations in macroscopic properties. From structural investigations of the Nafion® ionomer, it is known that the hydrophobic backbone is a continuous semicristalline region, meanwhile the hydrophilic sulfonic groups are organized in clusters that can incorporate water and allow for ions/protons and water transport. Hence, the water uptake is directly related to the size of these clusters [44]. Whereas commercial Nafion® 117 membrane is prepared by extrusion, the Nafion™ NR50 based membranes are herein obtained by casting from a diluted solution of NR50 superacid resin in DMF. Due to the higher affinity of DMF for the Teflon backbone, the NR50 nanoaggregates in DMF assume a coiled-like shape where the sulfonated groups are buried inside, in order to minimize the interfacial contact with the solvent. Such conformational

arrangement, also dependant on the nature of the casting substrate, leads to a random distribution of the hydrophobic and hydrophilic domains that prevents the formation of large clusters. In fact, the lower water uptake properties and the higher SCA values registered for NR50 Flat sample (i.e. 77.7±4.4° when compared to 117 Flat, i.e. 64.7±2.9°) may be attributed to changes in the spatial organization of the Nafion nanoaggregates. Figure 8.b displays the C1s core level spectra of 117 Flat and NR50 Flat samples, respectively. Unlike 117 Nafion, the contribution of fluorinated carbon atoms on the surface of NR50 is predominant. In addition, a new shoulder centered at 284.9 eV, ascribed to carbon atoms bonded to hydroxyl groups, is observed. Thus, XPS results are supporting our hypothesis about conformational changes in Nafion induced by the preparation conditions of the membranes.

From the experimental SCA (θ) values reported in Figure 9, it is clearly noticeable the change in wettability of the patterned membranes when compared to the flat counterparts of the same Nafion type. For hydrophobic NR50 based membranes, the patterning on the surface induce larger contact angle. In contrast, a larger wetting tendency (lower SCA values) is observed with patterning on the hydrophilic 117 based membranes.

To gain insight the wetting behaviour of the protein solution during crystallization process, the apparent SCA values assuming either homogeneous, i.e. Wenzel equation (1), or heterogeneous, i.e. Cassie Baxter equation (2), equilibrium wetting conditions [45], were also calculated:

$$\Gamma \cos\theta_Y = \cos\theta \quad (1)$$

Where Γ represents the ratio between the actual surface area and the projected surface area and θy represents the ideal Young contact angle (contact angle for 117 flat or NR50 flat samples).

$$\cos\theta \quad = f_{solid} \cos\theta_Y - f_{air} \quad (2)$$

Where f_{solid} is the fraction area of the top surface of the membrane, θ_Y is the ideal Young contact angle and f_{air} is the fraction area of the wells.

These values, assuming the topological information provided by SEM images, are comparatively shown with the experimental results in Table 2.

Table 2. Wettability of the Nafion® based membranes studied in this work.

Name	Ra (nm)	Experimental SCA(θ)	Apparent SCA (Wenzel)	Apparent SCA (Cassie-Baxter)	CCA (θ_c)
117 Flat	1.0±0.2	64.7 ±2.9	n.a.	n.a.	n.a.
117 Nano	14.9±4.9	63±2.4	54	80	109
117 Micro	4.0±0.4	48±4.2	42	80	101
NR50 Flat	n.a.	77±4.4	n.a.	n.a.	n.a.
NR50 Micro	2.8±0.4	100±4	69	90	101
Hierarchical	4.52	87±4.6	70	75	102

It is worthy to mention that the nanoscopic roughness values, Ra, evaluated by AFM and shown in Table 1 are not herein considered. In general, the experimental SCA results of patterned 117 membranes are well predicted by the homogeneous Wenzel model. Instead, in the case of the NR50 set, the experimental results are closer to the heterogeneous Cassie-Baxter theory, characteristic of composite solid-air surfaces with heterogeneous wetting, i.e. the drop lying on the top of the patterned surface.

In addition, the critical contact angle CCA (θ_c) was calculated as follows:

$$\cos\theta_c = -\frac{1-f_{solid}}{\Gamma-f_{solid}} \quad (3)$$

When $\theta_Y < \theta_c$ the Wenzel state is energetically more favourable; however, a metastable Cassie-Baxter state could still be possible [44]. Based on the CCA calculations, all the Nafion membranes studied in this work fulfilled the Wenzel state condition: $\theta_Y<\theta_c$; although NR50 set experimentally behaves closer to the heterogeneous Cassie-Baxter model. We attribute this observation to the use of a PDMS mold in the REM (NR50 Micro) or MT (Hierarchical) processes. Owing to the two distinct moieties of the Nafion ionomer: the hydrophobic backbone and hydrophilic sulfonic group; interaction of Nafion with highly hydrophobic PDMS surfaces is possible. Thus, the Nafion nanoaggregates could orientate at the interface in contact with the elastomeric mold to facilitate the interaction between the hydrophobic backbone of the ionomer and the hydrophobic PDMS mold (SCA = 125˚±0.6); meanwhile the sulfonic groups would be pointing away from the interfacial layer. In our opinion, such

interfacial interaction provokes the modification of the fine structure of Nafion in close vicinity to the replicated features, i.e. altering the distribution of water-filled ionic domains and influences its surface tension properties and wetting regime. On the contrary, the micro and nano hard molds used for the imprinting of Nafion ® 117 membranes were hydrophilic.

Impact of surface patterning on protein crystallization

The patterned Nafion® membranes, both 117 and NR50 types, were tested for the crystallization of Trypsin from Bovine Pancreas. The crystallization and precipitant solutions were mixed on the top of the nucleant membranes (0.7 cm x 0.7 cm) and left equilibrating with the stripping solution in a closed system. The experiments were performed in adapted crystallization well plates and followed over time by optical microscopy. Optical images of the crystals are shown in Figure 10.

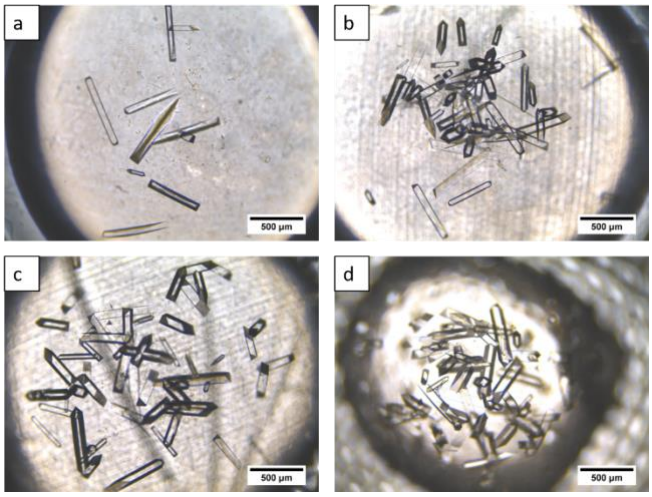

Figure 10. Optical images of crystals grown on the patterned membranes. a) 117-Flat b) 117-Nano c) 117-Micro d) Hierarchical.

Results of nucleation and growth rate are reported in Figure 11 and Figure 12, respectively. From those data, crystallization parameters such as induction time, nucleation and growth rate were calculated (see Table 3). The induction time was extrapolated from the intersection point of the curves in Figure 11 with the axis of time, whereas nucleation and growth rate values, were calculated as the first derivative at the time axis intersection of the curves of Figure 11 and Figure 12, respectively.

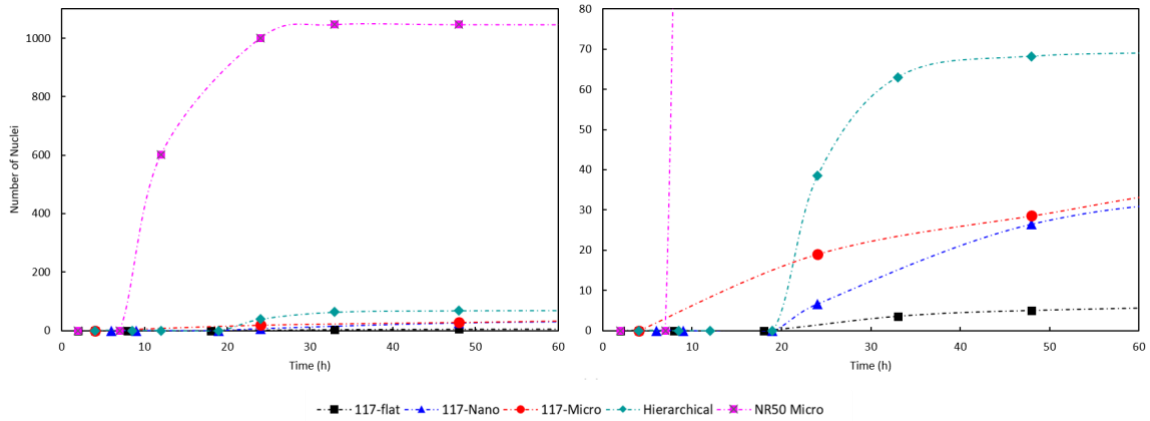

Figure 11 Number of crystals observed versus time for the nucleant membranes studied in this work. On the left side it is shown the evolution of the number of crystals as a function of time for all the patterned membranes. On the right side a magnification of the down area of the graph is displayed.

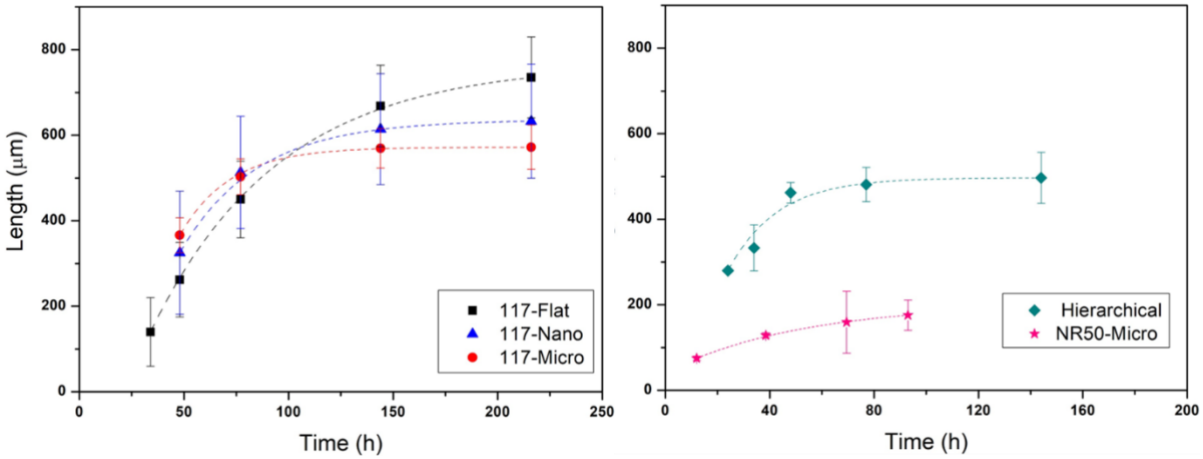

Figure 12. Length of crystals observed versus time for the nucleant membranes studied in this work.

Table 3. Estimated values of induction time, nucleation rate and growth rate for the different membranes studied in this work for the different membranes studied in this work.

Name	Ra (nm)	Experimental SCA (θ)	Estimated Induction Time (h)	Nucleation rate (nuclei/h)	Crystal Growth rate (µm/h)
117 Flat	1.0±0.2	64.7 ±2.9	18	0.3±0.1	12.0±0.4
117 Nano	14.9±4.9	63±2.4	19	1.5±0.2	20.0±1.2
117 Micro	4.0±0.4	48±4.2	4	1.3±0.6	21.8±0.8
NR50 Micro	2.8±0.4	100±4	7	198.5±8.0	12.9±0.4
Hierarchical	4.52	87±4.6	19	11.3±0.4	25.8±13.9

In general, all the patterned Nafion® membranes demonstrate an increase of the nucleation rate and crystal growth when compared to the control sample. The reported results may be explained following both the classical and the two-step nucleation theory.

Two-step Nucleation Theory

Changes from a liquid to a crystalline solid phase are associated to changes of two main parameters: concentration of the solute and structure of the solid formed. According to the two-step nucleation theory, the process might be energetically more favourable if these changes occur in a sequence order (two-steps). In particular, firstly a highly dense amorphous cluster with a significantly higher protein concentration compared to the bulk is formed (concentration change) and later, after crossing the free energy barrier, a crystalline nucleus is formed inside the dense cluster (structural change) (Figure 13) [4,47].

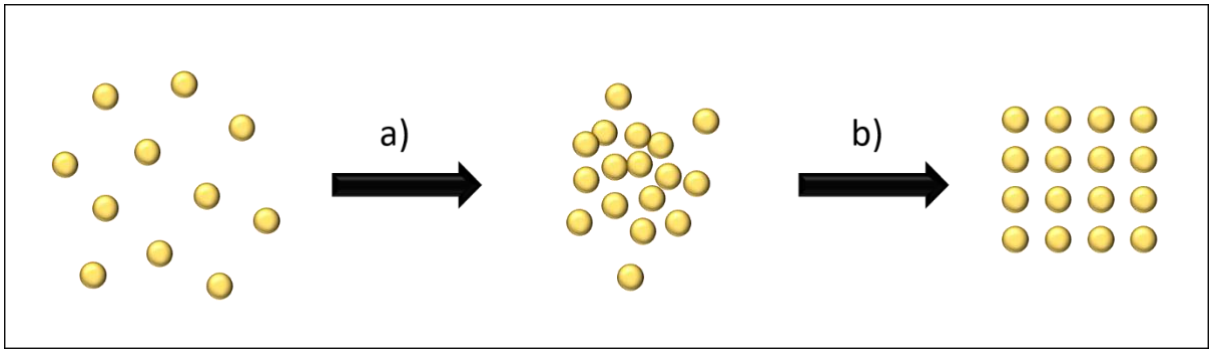

Figure 13 Two-step mechanism: a) Formation of dense cluster; b) Organization of the dense cluster in a crystalline nucleus.

The 117-Nano membrane is characterized by the presence of nanowells. The probability for a molecule to enter into a narrow space (up to 1000 nm) is the same as on a flat surface, however, due to the Brownian motion, escaping from a narrow space may result much more difficult determining physical entrapment and local accumulation. When this event occurs over time, the concentration of molecules inside the well increases, determining the formation of dense clusters (first step). The higher protein concentration within the pores compared to bulk determines a very low Gibbs free energy with consequent formation of the crystalline phase inside the pores (second step) and the formation of extra nucleation

sites outside the nanopores (see Figure 14) [48]. The size of Trypsin crystal unit cell (that considers also the void space between the monomers) is 5.4 nm x 5.9 nm x 6.6 nm [47], thus the total volume of one monomer unit is 212 nm^3. Accordingly, the number of unit cells that could fit in a nanowell is approximately 2500 (assuming a pore volume of 5.3 x 10^5 nm^3)

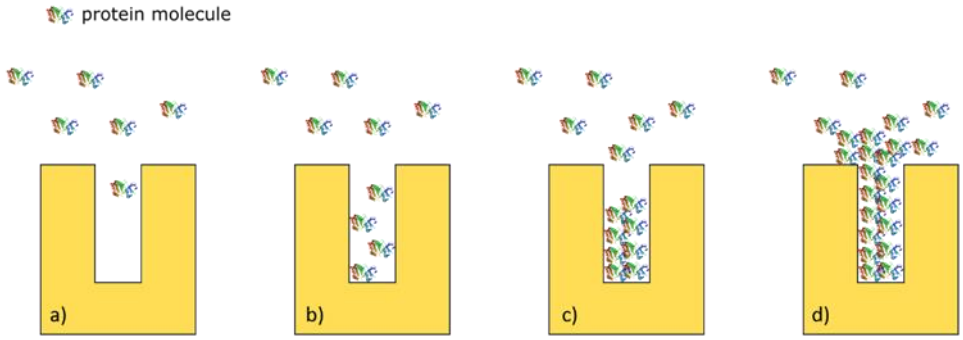

Figure 14. Proposed nucleation mechanism in a narrow cavity: a) the probability of a protein molecule of entering in a narrow cavity is the same as on the top of the surface; b) the narrow cavity determines entrapment of the protein molecules that will consequently accumulate over time; c) the increased concentration inside the pore promotes nucleation; d) the top surface of a cavity filled with a nucleus becomes a nucleation point for crystal growth outside the pore.

In the case of 117-Micro, the spreading of the solution on the nucleant surface (notice the decrease of the contact to SCA=48±4.2 °) generates a higher ratio between actual and projected area, which means higher contact area between the surface and the protein solution that may promote stabilization of the dense clusters (first step) and later nucleation (second step). On the contrary, when looking at the induction time in Table 3, there is not a clear apparent correlation with membrane topography. It is well reported that not only the surface topography, but also the amount of interactive sites and the enhanced adhesion of the protein solution affect the nucleation phenomena to different extent. In fact, 117 Nano does not show any improvement on induction time compared to 117 Flat, i.e. 19 h vs. 18 h; whereas 117 Micro displays a significant lower value, i.e. 4 h. This observation could be explained by the interfacial surface properties, as the micro-features have a significant effect on the SCA values. For both membranes, i.e. 117 Nano and 117 Micro, an increase in the nucleation sites number occurs. However, while in the case of 117 Micro this occurs

immediately, due to the higher wettability in the case of 117 Nano some time is required for accumulation of protein molecules inside the nanowells.

Regarding the NR50 Micro membrane, even though the microstructure is the same as the 117 Micro, the two membranes lead to completely different outputs. Indeed, even though the induction time is comparable, i.e. 7 h; the nucleation rate and final the number of crystals are the highest among the tested: 198±8 nuclei/h and 1046±100 crystals per NR50 Micro membrane unit, respectively. Protein adhesion due to the presence of the micro-features is enhanced by the distinctive hydrophobic character of the NR50 surface (SCA=100±4 °), °) which may lead to a reduced motility of the molecules, hence promoting the formation of a highly dense area in the proximity of the membrane (first step) and a high number of nuclei rapidly formed (second step). Due to the formation of this high number of nuclei in a short time, a lower amount of protein is available in the solution determining a slower growth rate compared to the hydrophilic membranes.

Finally, the hierarchical membrane (which is a hybrid membrane of NR50-Micro and 117-Nano) has an intermediate behaviour between the 117 Nano and the NR50 Micro membranes.

Modelling the Gibbs free energy of heterogeneous nucleation for the patterned Nafion based membranes

In order to discuss the effect of surface properties from the point of view of classical nucleation theory, an adaptation of the model developed by Liu et. al [18] including the effect of tailored surface topography in the evaluation of the ratio of heterogeneous to homogeneous nucleation has been developed. Theoretical calculations resulted from this model were compared with experimental results.

The free energy variation for heterogeneous nucleation (ΔG_{Het}) is defined as [48]:

$$\Delta G_{Het} = \Phi \Delta G_{Hom} \quad (4)$$

Where ϕ is the ratio of Gibbs free energy variation of heterogeneous to homogeneous nucleation and ΔG_{Hom} is the free energy variation for homogeneous nucleation. According to literature[18], for an ideally flat surface (without any patterning), Φ is defined as:

$$\Phi = \frac{2-3\cos\theta_Y+3\cos\theta_Y{}^3}{4} \quad (5)$$

Therefore, the main parameter affecting heterogeneous nucleation is the Young's contact angle θ_Y between the forming nucleus (assumed to be spherical) and the substrate that defines the area of interaction between the nucleus and the surface. In fact, surfaces with lower SCA lead to lower values of ϕ (ratio of Gibbs free energy variation of heterogeneous to homogeneous nucleation) according to Equation 5.

In order to include the effect of surface topography on Gibbs free energy variation of heterogeneous to homogeneous nucleation, Liu *et al*. [18] developed a model for rough surfaces, assuming: i) the surface to be composed by uniform cones; and ii) a Wenzel's wetting state. In this work, Liu model has been adapted to the geometry of the topography of the patterned membranes herein studied and theoretical values are correlated with experimental results. Thus, on the top of the substrate, a nucleus with a hypothetical round shape of radius R contacting the substrate with an apparent contact angle θ is considered (see Figure 15).

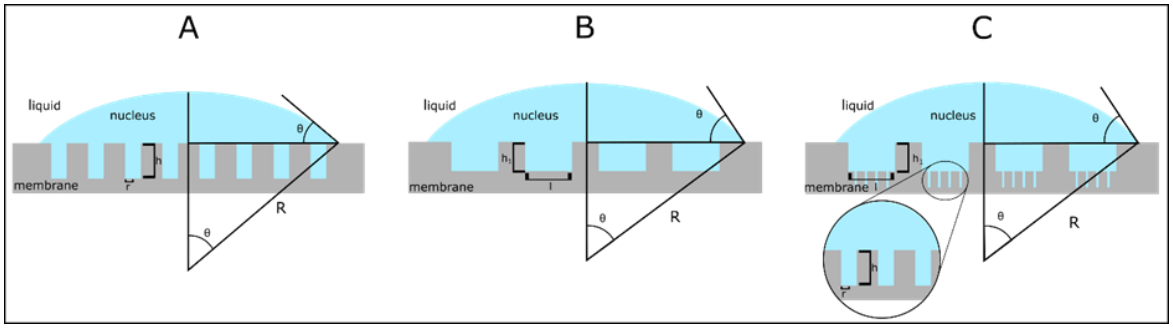

Figure 15. Diagram of the geometry parameters of a surface with cylindrical wells used for ΔG_{Het} calculations.

Details on the derivation of the equations are reported in the Supporting Information. For the 117-Nano membrane the equation obtained was the following:

$$\Phi_{117-Nano} = \frac{\Delta G^*_{Het}}{\Delta G^*_{Hom}} = \frac{1}{4}\frac{[2(1-\cos\theta)-\cos\theta\sin\theta^2]^3}{[(1-\cos\theta)^2(2+\cos\theta)+3n\alpha^2\beta]^2} \quad (6)$$

Where , r is the radius of the cylindrical wells, n is the number of wells under the area of the nucleus, θ is the apparent contact angle between the nucleus and the surface (Figure 15 A), $\alpha = \frac{r}{R}, \beta = \frac{h}{R}$.

For 117 Micro and NR50 Micro the equation used was the following:

$$\Phi_{Micro} = \frac{\Delta G^*_{Het}}{\Delta G^*_{Hom}} = \frac{1}{4}\frac{\pi^2[2(1-\cos\theta)-\cos\theta\sin\theta^2]^3}{[\pi(1-\cos\theta)^2(2+\cos\theta)+\frac{3}{2}\sqrt{3}n_1{\alpha_1}^2\beta_1]^2} \quad (7)$$

Where l is the side of the triangle base of the prism-shaped well, h_1 is the depth, n_1 is the number of wells under the area of the nucleus, θ is the apparent contact angle between the nucleus and the surface (Figure 15 B), $\alpha_1 = \frac{l}{R}$, $\beta_1 = \frac{h_1}{R}$.

For the Hierarchical membrane the equation used was the following:

$$\Phi_{Hierarchical} = \frac{\Delta G^*_{Het}}{\Delta G^*_{Hom}} = \frac{1}{4}\frac{\pi^2[2(1-\cos\theta)-\cos\theta\sin\theta^2]^3}{[\pi(1-\cos\theta)^2(2+\cos\theta)+\frac{3}{2}\sqrt{3}n_1{\alpha_1}^2\beta_1+3n\alpha^2\beta]^2} \quad (8)$$

Where l is the side of the triangle base of the prism-shaped well and h_1 is the depth, n_1 is the number of wells under the area of the nucleus, r is the radius of the wells, n is the number of nanowells inside a microwell, θ is the apparent contact angle between the nucleus and the surface (Figure 15 C).

Accordingly, the ratio of the Gibbs free energy of heterogeneous nucleation to homogeneous nucleation, ϕ, has been calculated from equations 5, 6, 7 and 8 for each membrane (see Table 4).

Table 2 Ratio of the Gibbs free energy variation of heterogeneous nucleation to homogeneous nucleation

Name	$\frac{\Delta G_{Het}}{\Delta G_{Hom}} = \Phi$
117 Flat	0.19
117 Nano	0.18
117 Micro	0.07
NR50 Micro	0.52
Hierarchical	0.45

It is worthy to mention that the nanoscopic roughness values, Ra, evaluated by AFM and shown in Table 1 are not accounted for the model. As expected, the Gibbs free energy of nucleation is always reduced in presence of Nafion type nucleant surface. In addition, 117 Nafion® type membranes induce the highest reduction in ϕ. This decrease is much higher for the 117 Micro compared to 117 Nano in agreement with heterogeneous nucleation theory: surfaces with lower contact angles, hence with high degree of hydrophilicity, favour nucleation of proteins [11,18]. Indeed, a lower contact angle means a wider spreading of the solution on the top of the surface increasing the contact area for the same volume of solution, and thus the local concentration of solute molecules, lowering the energy barrier for nucleation.

The higher value of Gibbs free energy for heterogenous nucleation for NR50 and Hierarchical membrane compared to 117 membrane set can be attributed to their hydrophobic character. Indeed, according to Liu model, the hydrophobic character increases the energy barrier for nucleation due to a lesser area of interaction between the crystallization solution and the surface. This seems to be the case when comparing ϕ for 117 Micro and NR50 Micro samples (0.07 vs. 0.52), which have exactly the same geometry, although with different interfacial properties.

When comparing kinetics, a significantly higher number of nuclei per unit time is obtained for NR50 Micro than for 117-Micro: 198.52±7.96 vs. 1.31±0.61. Furthermore, the number of crystals recorded at equilibrium conditions is also superior, although lower in size, for NR50 Micro nucleant membrane: 175±103 vs. 571±126. We attribute this behaviour to the more predominant role of the surface chemistry and interfacial interactions. Due to ionomeric nature of Nafion and the different fabrication conditions (temperature, solvent, mold nature), 117 and NR50 membranes show different polymer chains organization that leads to different surface properties. In the NR50 membrane the hydrophilic groups are buried inside, enhancing the hydrophobic character of the surface which promotes stronger protein-surface interactions, less motility and consequently higher nucleation rate.

Above all, the model developed by Liu et al. does not consider the contribution of interfacial interactions to the Gibbs free energy heterogeneous nucleation. Furthermore, it is based on the simplified assumption that the liquid phase is following the homogeneous Wenzel

regime for all the contacting surface and, as previously discussed, metastable Cassie-Baxter state may occur in the case of NR50 membranes.

Guidelines for designing membrane topographies for improved nucleation and crystallization

Nucleation is a probability event; hence different conditions lead to different chances of obtaining crystals. Enhancing the probability for this phenomenon to occur is extremely important for increasing the possibility of obtaining well-diffracting crystals, especially in the case of protein molecules difficult to nucleate.

Designing of specific surface topography membranes demonstrated to have an impact on the crystallization process. However, predicting which type of surface topography may promote a more effective nucleation is not obvious and simple.

Taking into account the results of this work, we would like to draw guidelines for designing surfaces suitable for nucleation and crystallization of proteins:

1) Small features, in the nano size range, lead to higher nucleation due to the creation of extra nucleation sites by physical entrapment. Hence, they might be particularly useful for implementing nucleation on membranes whose surface properties do not favour nucleation.
2) Micro-scale features on highly hydrophilic surfaces induce an increase in the wettability and consequently in the surface/volume ratio enhancing the effect of the chemistry of the material. Hence, they can be useful to improve the crystallization output on membranes with surface properties that favour the nucleation process.
3) Micro-scale features on hydrophobic surfaces induce a further decrease in the wettability and may lead to higher protein-surface interactions with a much stronger effect on nucleation compared to hydrophilic surfaces carrying the same features.

Hence, depending on the chemistry of the surface, the interfacial interactions with the growing nuclei and its effect on nucleation and crystallization, it is possible to decide the best strategy for introducing small or large features, or both, in order to control the number of nuclei and the final size of the crystals.

Theoretical calculations based on the model developed by Liu et al. help in predicting the effect of a defined geometry on nucleation rate; however, this model presents some obvious limitations. The model relies on the Wenzel equation and the surface/volume ratio (described by the contact angle) is considered the main controlling factor for protein nucleation on the membrane surface. This applies only for hydrophilic surfaces with a high Γ (ratio between actual and projected area). In the case of small surface features, which do not have a strong effect on the contact angle, or more hydrophobic surfaces where the solution does not follow the homogeneous Wenzel regime, other phenomena such as physical entrapment and chemical interactions at the interface might occur playing a significant role, that are not taken into consideration by the Liu *et al.* model.

Therefore, a refined theoretical approach including the fluid dynamics of the protein solution contacting specific nano cavities and protein-surface interactions at the interface should be accounted for a model closer to reality.

Conclusions

Controlling heterogeneous nucleation by surface topography can be regarded as a very effective way to handle the complex process of protein crystallization. So far, modifications of the surface topography were always associated with chemical modifications, making difficult a comparison with a flat surface. What emerged from previous investigations was that an incremented nucleation activity could be observed for surfaces with increased roughness.

In this work, Nafion® membranes were processed with low cost and high-throughput soft lithographic techniques in order to create periodic surface topographies with different sizes (micro, nano and a combination of both) in an attempt to minimize the surface chemistry changes and to study in detail the specific effect of topography on the nucleation process. However, the ionomeric nature of Nafion, although beneficial for fast transport of ions and water, has imposed several constraints when trying to preserve unaltered its interfacial properties whatever the membrane processing strategy used.

The results obtained with Trypsin showed, as expected, an increased nucleation activity and crystal grow rate for all the patterned membranes. It was also shown that membranes with the same topography but prepared by following different routes might result in a different crystallization output. This fact is an indication that different nucleation mechanisms might occur, depending not only on the size of the topographical features but also on the surface properties of the membrane and on the contribution of interfacial interactions. All the patterned Nafion® based membranes obey an asymptotic tendency when analysing the dimensions and size of the collected Trypsin crystals: the higher number of crystals the lower in size. Thus, the production of macroscopic Trypsin crystals with tuneable size distribution would be feasible by a proper selection of the nucleant membrane topography.

Some obvious limitations arise when the experimental crystallization results were analysed in view of the ratio of the Gibbs free energy variation of heterogeneous nucleation to homogeneous nucleation (ϕ) predicted from the Liu model. Additional phenomena, such as the local accumulation of protein molecules in a restricted space and protein-surface interactions at the interface are playing a key role on heterogeneous nucleation and growth.

Acknowledgements

This work was supported by the Associate Laboratory for Green Chemistry- LAQV which is financed by national funds from FCT/MCTES (UID/QUI/50006/2019). Mariella Polino would like to thank the Education, Audiovisual and Culture Executive Agency (EACEA) for the Ph.D. grant under the Program “Erasmus Mundus Doctorate in Membrane Engineering” – EUDIME (FPA 2011-2014, http://www.eudime.unical.it). The microscopy images have been recorded in the Laboratorio de Microscopias Avanzadas at Instituto de Nanociencia de Aragon-Universidad de Zaragoza. Authors acknowledge the LMA-INA for offering access to their SEM and XPS instruments and expertise.

Supporting information

The supporting information provides additional characterization of imprinted membranes, details on the fabrication of the molds used for replica molding and the free Gibbs energy calculations derived from the Classical Nucleation.

References

[1] J.A. Gavira, Current trends in protein crystallization, Arch. Biochem. Biophys. 602 (2016) 3–11.

[2] R. Giegé, A historical perspective on protein crystallization from 1840 to the present day, FEBS J. 280 (2013) 6456–6497.

[3] J.M. Garcia, Nucleation of protein crystals, J. Struct. Biol. 142 (2003) 22–31.

[4] P.G. Vekilov, Nucleation of protein crystals, Prog. Cryst. Growth Charact. Mater. 62 (2016) 136–154.

[5] R.-B. Zhou, H.-L. Cao, C.-Y. Zhang, D.-C. Yin, A review on recent advances for nucleants and nucleation in protein crystallization, CrystEngComm. 19 (2017) 1143–1155.

[6] A. Mcpherson, P. Shlichta, Heterogeneous and Epitaxial Nucleation of Protein Crystals on Mineral Surfaces, Science (80-.). 239 (1988) 385–387.

[7] A. Gugliuzza, C. Aceto, E. Drioli, Interactive functional poly (vinylidene fluoride) membranes with modulated lysozyme affinity : a promising class of new interfaces for contactor crystallizers, Polym Int. 58 (2009) 1452–1464.

[8] C. Zhang, H. Shen, Q. Wang, Y. Guo, J. He, An Investigation of the Effects of Self-Assembled Monolayers on Protein Crystallisation, Int. J. Mol. Sci. 14 (2013) 12329–12345.

[9] D.S. Tsekova, D.R. Williams Nn, J.Y.Y. Heng, Effect of surface chemistry of novel templates on crystallization of proteins, Chem. Eng. Sci. 77 (2012) 201–206.

[10] T. Pham, D. Lai, D. Ji, W. Tuntiwechapikul, J.M. Friedman, T.R. Lee, Well-ordered self-assembled monolayer surfaces can be used to enhance the growth of protein crystals, Colloids Surfaces B Biointerfaces. 34 (2004) 191–196.

[11] E. Curcio, E. Fontananova, G. Di Profio, E. Drioli, Influence of the structural properties of poly(vinylidene fluoride) membranes on the heterogeneous nucleation rate of protein crystals., J. Phys. Chem. B. 110 (2006) 12438–45.

[12] U. V Shah, C. Amberg, Y. Diao, Z. Yang, J.Y. Heng, Heterogeneous nucleants for crystallogenesis and bioseparation, Curr. Opin. Chem. Eng. 8 (2015) 69–75.

[13] U. V. Shah, N.H. Jahn, S. Huang, Z. Yang, D.R. Williams, J.Y.Y. Heng, Crystallisation via novel 3D nanotemplates as a tool for protein purification and bio-separation, J. Cryst.

Growth. 469 (2017) 42–47.

[14] U. V. Shah, M.C. Allenby, D.R. Williams, J.Y.Y. Heng, Crystallization of proteins at ultralow supersaturations using novel three-dimensional nanotemplates, Cryst. Growth Des. 12 (2012) 1772–1777.

[15] U. V. Shah, D.R. Williams, J.Y.Y. Heng, Selective crystallization of proteins using engineered nanonucleants, Cryst. Growth Des. 12 (2012) 1362–1369.

[16] A.S. Ghatak, A. Ghatak, Precipitantless Crystallization of Protein Molecules Induced by High Surface Potential, Cryst. Growth Des. 16 (2016) 5323–5329.

[17] A.S. Ghatak, G. Rawal, A. Ghatak, Precipitant-Free Crystallization of Protein Molecules Induced by Incision on Substrate, Crystals. 7 (2017) 245.

[18] Y.-X. Liu, X.-J. Wang, J. Lu, C.-B. Ching, Influence of the Roughness, Topography, and Physicochemical Properties of Chemically Modified Surfaces on the Heterogeneous Nucleation of Protein Crystals, J. Phys. Chem. B. 111 (2007) 13971–13978.

[19] W. De Poel, J.A.W. Mü, J.A.A.W. Elemans, W.J.P. Van Enckevort, A.E. Rowan, E. Vlieg, Surfaces with Controllable Topography and Chemistry Used as a Template for Protein Crystallization, Cryst. Growth Des. 18 (2018) 763–769.

[20] H. Hou, B. Wang, S.-Y. Hu, M.-Y. Wang, J. Feng, P.-P. Xie, D.-C. Yin, An investigation on the effect of surface roughness of crystallization plate on protein crystallization, J. Cryst. Growth. 468 (2017) 290–294.

[21] E. Chabanon, D. Mangin, C. Charcosset, Membranes and crystallization processes: State of the art and prospects, J. Memb. Sci. 509 (2016) 57–67.

[22] E. Drioli, G. Di Profio, E. Curcio, W.S.W. Ho, K. Li, Progress in membrane crystallization, Curr. Opin. Chem. Eng. 1 (2012) 178–182.

[23] X. Zhou, X. Zhu, B. Wang, J. Li, Q. Liu, X. Gao, K.K. Sirkar, D. Chen, Continuous production of drug nanocrystals by porous hollow fiber-based anti-solvent crystallization, J. Memb. Sci. 564 (2018) 682–690.

[24] D. Chen, B. Wang, K.K. Sirkar, Hydrodynamic modeling of porous hollow fiber anti-solvent crystallizer for continuous production of drug crystals, J. Memb. Sci. 556 (2018) 185–195.

[25] J. Motuzas, C. Yacou, R.S.K. Madsen, W. Fu, D.K. Wang, A. Julbe, J. Vaughan, J.C. Diniz da Costa, Novel inorganic membrane for the percrystallization of mineral, food and pharmaceutical compounds, J. Memb. Sci. 550 (2018) 407–415.

[26] G. Di Profio, M. Polino, F.P. Nicoletta, B.D. Belviso, R. Caliandro, E. Fontananova, G. De Filpo, E. Curcio, E. Drioli, Tailored hydrogel membranes for efficient protein crystallization, Adv. Funct. Mater. 24 (2014) 1582–1590.

[27] S.M. Salehi, A.C. Manjua, B.D. Belviso, C.A.M. Portugal, I.M. Coelhoso, V. Mirabelli, E. Fontananova, R. Caliandro, G. João, Crespo, E. Curcio, G. Di Profio, Hydrogel Composite Membranes Incorporating Iron Oxide Nanoparticles as Topographical

Designers for Controlled Heteronucleation of Proteins, Cryst. Growth Des. 18 (2018) 3317–3327.

[28] D. Qin, Y. Xia, G.M. Whitesides, Soft lithography for micro- and nanoscale patterning, Nat. Protoc. 5 (2010) 491–502.

[29] T. Glinsner, G. Kreindl, 24 Nanoimprint Lithography, Lithography. 24 (2010) 495–516.

[30] A. Fernandez, J. Medina, C. Benkel, M. Guttmann, B. Bilenberg, L.H. Thamdrup, T. Nielsen, C.M. Sotomayor Torres, N. Kehagias, Residual layer-free Reverse Nanoimprint Lithography on silicon and metal-coated substrates, Microelectron. Eng. 141 (2015) 56–61.

[31] B. Radha, S.H. Lim, M.S.M. Saifullah, G.U. Kulkarni, Metal hierarchical patterning by direct nanoimprint lithography, Sci. Rep. 3 (2013) 1078.

[32] M. Polino, A. Luísa Carvalho, L. Juknaite, C.A. M Portugal, I.M. Coelhoso, M.J. Romao, J.G. Crespo, Ion-Exchange Membranes for Stable Derivatization of Protein Crystals, Cryst. Growth Des. 17 (2017) 4563–4572.

[33] J. Mótyán, F. Tóth, J. Tőzsér, Research Applications of Proteolytic Enzymes in Molecular Biology, Biomolecules. 3 (2013) 923–942.

[34] H.A.M. Mönttinen, J.J. Ravantti, M.M. Poranen, Structural comparison strengthens the higher-order classification of proteases related to chymotrypsin, PLoS One. 14 (2019) 1–16.

[35] A. Laskar, E.J. Rodger, A. Chatterjee, C. Mandal, Modeling and structural analysis of PA clan serine proteases, BMC Res. Notes. 5 (2012) 1.

[36] C.-H. Ma, T.L. Yu, H.-L. Lin, Y.-T. Huang, Y.-L. Chen, U.-S. Jeng, Y.-H. Lai, Y.-S. Sun, Morphology and properties of Nafion membranes prepared by solution casting, Polymer (Guildf). 50 (2009) 1764–1777.

[37] H. Le-the, E. Berenschot, R.M. Tiggelaar, N.R. Tas, A. Van Den Berg, J.C.T. Eijkel, Shrinkage Control of Photoresist for Large-Area Fabrication of Sub-30 nm Periodic Nanocolumns, Adv. Mater. Technol. (2017).

[38] A. Pimpin, W. Srituravanich, Review on Micro- and Nanolithography Techniques and their Applications, Eng. J. 16 (2012) 37–55.

[39] P.K. David Neˇ cas, Gwyddion : an open-source software for SPM data analysis, Cent. Euopean J. Phys. 10 (2012) 181–188.

[40] C.A. Schneider, W.S. Rasband, K.W. Eliceiri, NIH Image to ImageJ: 25 years of image analysis, Nat. Methods. 9 (2012) 671–675.

[41] I. Khan, K.A. Kurnia, F. Mutelet, S.P. Pinho, J.A.P. Coutinho, Probing the interactions between ionic liquids and water: Experimental and quantum chemical approach, J. Phys. Chem. B. 118 (2014) 1848–1860.

[42] H. Jung, J. Won, Role of the glass transition temperature of Nafion 117 membrane in

the preparation of the membrane electrode assembly in a direct methanol fuel cell (DMFC), Int. J. Hydrogen Energy. 37 (2012) 12580–12585.

[43] S.H. de Almeida, Y. Kawano, Thermal Behavior of Nafion Membrane, J. Therm. Anal. Calorim. 58 (1999) 569–577.

[44] K.A. Mauritz, R.B. Moore, State of Understanding of Nafion, Chem. Rev. 104 (2004) 4535–4585.

[45] E. Celia, T. Darmanin, E.T. De Givenchy, S. Amigoni, F. Guittard, Recent advances in designing superhydrophobic surfaces, J. Colloid Interface Sci. 402 (2013) 1–18.

[46] P. Esa, R. Tiina, S. Mika, A.P. Tapani, Superhydrophobic Polyolefin Surfaces: Controlled Micro- and Nanostructures, Langmuir. 23 (2007) 7263–7268.

[47] D. Erdemir, A.Y. Lee, A.S. Myerson, Nucleation of crystals from solution: Classical and two-step models, Acc. Chem. Res. 42 (2009) 621–629.

[48] C.N. Nanev, E. Saridakis, N.E. Chayen, Protein crystal nucleation in pores, Sci. Rep. 7 (2017) 35821–35829.

[49] J.A. Garcia-Granda, S.; Chamorro Gavilanes, Native Bovine Pancreatic Trypsin. Preliminary Full wwPDB X-ray Structure Validation Report, 2018.

[50] T.E. Paxton, A. Sambanis, R.W. Rousseau, Influence of vessel surfaces on the nucleation of protein crystals, Langmuir. 17 (2001) 3076–3079.

For Table of Contents Use Only

Enhanced protein crystallization on Nafion® membranes modified by low-cost surface patterning techniques

M. Polino [1], C. A. M. Portugal [1], H. Le The [2], R. Tiggelaar [3], J. Eijkel [2], J. G. Crespo [1], I. M. Coelhoso [1]*, M. P. Pina [4, 5]*, R. Mallada [4, 5]

[1] LAQV-REQUIMTE/CQFB, Department of Chemistry, FCT/Universidade Nova de Lisboa, Portugal

[2] BIOS Lab-on-a-Chip, MESA+ Institute for Nanotechnology, University of Twente, The Netherlands

[3] NanoLab Cleanroom, MESA+ Institute for Nanotechnology, University of Twente, The Netherlands

[4] Nanoscience Institute of Aragon (INA), Instituto de Ciencia de Materiales de Aragon (ICMA), Department of Chemical and Environmental Engineering, Universidad de Zaragoza, Spain

[5] Instituto de Ciencia de Materiales de Aragon (ICMA), Universidad de Zaragoza-CSIC, Zaragoza, Spain

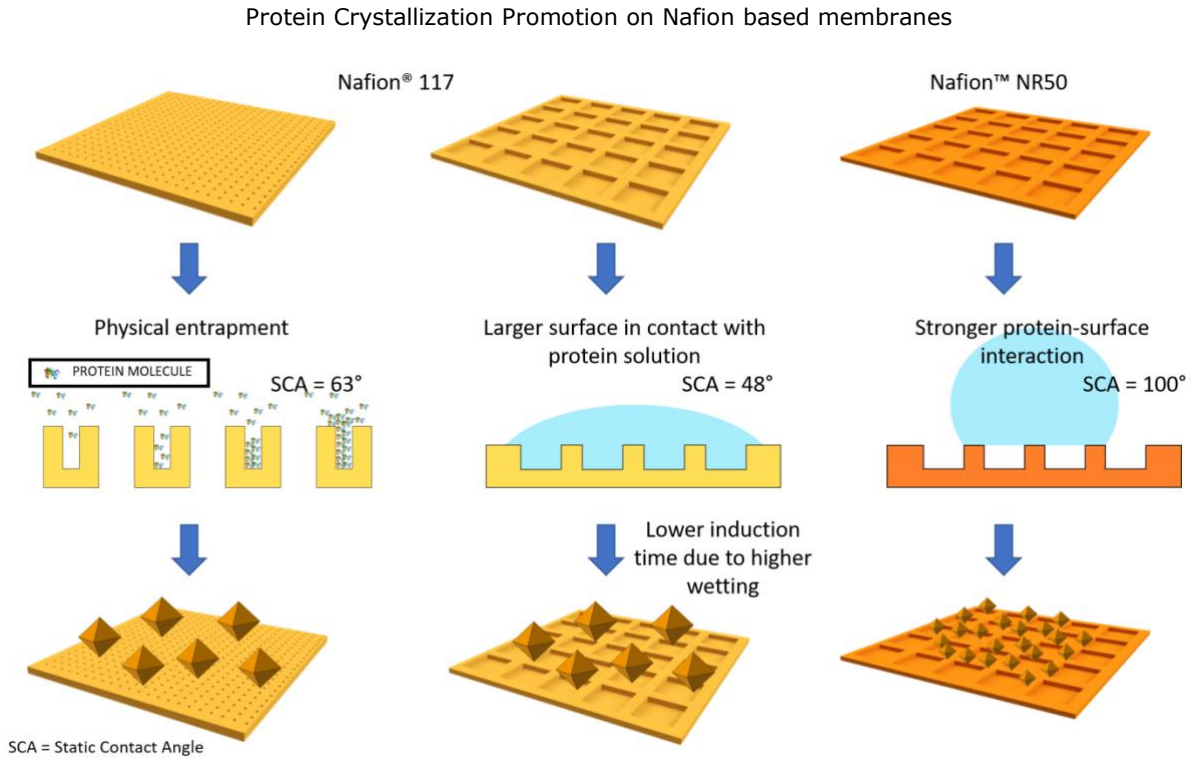

Periodic surface topographies with different sizes (micro, nano and a combination of both) are investigated on Nafion based membranes to study in detail the effect of topography on the nucleation activity and crystal grow rate of Trypsin protein, widely used in various biotechnological processes and food industry.

Enhanced protein crystallization on Nafion® membranes modified by low-cost surface patterning techniques

M. Polino [1], C. A. M. Portugal [1], H. Le The [2], R. Tiggelaar [3], J. Eijkel [2], J. G. Crespo [1], I. M. Coelhoso [1], M. P. Pina [4,5]*, R. Mallada [4,5]*

[1] LAQV-REQUIMTE/CQFB, Department of Chemistry, FCT/Universidade Nova de Lisboa, Portugal

[2] BIOS Lab-on-a-Chip, MESA+ Institute for Nanotechnology, University of Twente, The Netherlands

[3] NanoLab Cleanroom, MESA+ Institute for Nanotechnology, University of Twente, The Netherlands

[4] Nanoscience Institute of Aragon (INA), Instituto de Ciencia de Materiales de Aragon (ICMA), Department of Chemical and Environmental Engineering, Universidad de Zaragoza, Spain

[5] Instituto de Ciencia de Materiales de Aragon (ICMA), Universidad de Zaragoza-CSIC, Zaragoza, Spain

*Corresponding authors: imrc@fct.unl.pt; mapina@unizar.es

Keywords: Nafion membrane; soft lithography; surface topography; interfacial interactions; crystallization

Supporting Information

Nafion® structure

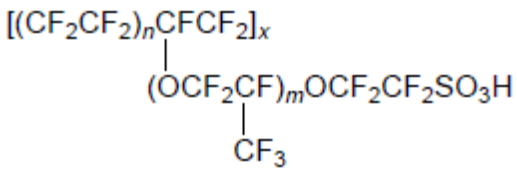

where *m*) 1, 2, or 3, and *n* typically has a value of about 6-7. For EW=1100g/eq m=1.

Definition of Imprinting Temperature by Differential Scanning Calorimetry

Thermal Nanoimprint Lithography (or hot embossing) transfers a pattern from a mould to a thermoplastic substrate. The process is commonly performed by heating the material to be imprinted at a temperature 20-50°C higher than the glass transition temperature (Tg) of the substrate and afterwards high pressure is applied to improve the contact between the mold and the substrate. Therefore, in order to assess the conditions for a successful imprinting, the Tg of Nafion® was determined by DSC analysis. The measurements were performed within a temperature interval of 35-250 °C, with a heating rate of 10°C/min. Since, according

to the literature [1,2,3], the water content of the polymer might affect the Tg because of plasticization effects, and Nafion® membranes easily change the water content according to environmental humidity variations, measurements were carried out for a range (from 0% to 24%) of water content of Nafion®. In order to control the membrane water content, membranes were left equilibrating in closed vessels with different saturated salt solutions (all conditions are reported in Table S1), and weight measured over time until no variation was recorded.

Table S1. Nafion® 117 samples equilibrated at different RH contents and water uptake values

Membrane	Water Uptake (%)
Nafion® 117 dried at 80°C	0
Untreated Nafion® 117	4.5
Nafion® 117 equilibrated with K_2CO_3 saturated solution RH=43%	9.8
Nafion® 117 equilibrated with KCl saturated solution RH=85%	18.4
Hydrated Nafion® 117	24.0

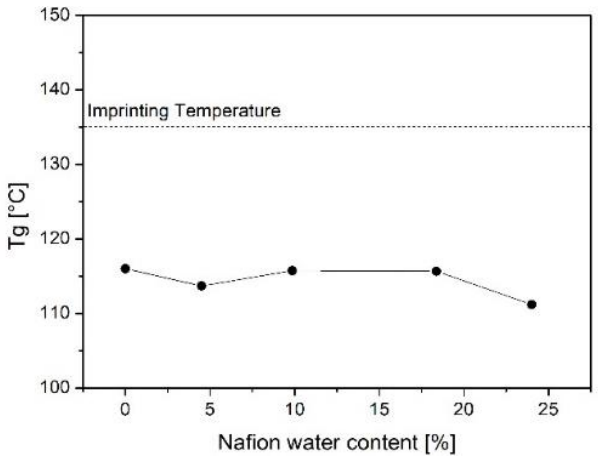

Figure S1. Glass transition temperature values of Nafion, estimated by DSC, as a function of its water content.

The results reported in Figure S1 show a Tg value of 114±2 and no significant differences were found for different water content of Nafion® 117. The Tg measured for this work is in

agreement with the values reported in the literature (115°C) [1,2]. In light of this result it was decided to perform the imprinting process at 135°C.

Fabrication of the SU8 micromold

The design (triangles with side 165 µm and repeating unit of 350 µm x 185 µm) has been made using the CleWin software (WieWeb software, Hengelo, NL) and transferred to a photolithography mask. A negative photoresist (SU-8 50 DE MicroChem) was spin-coated onto a Silicon wafer and exposed to UV light through the mask design in order to transfer the pattern onto the SU-8 layer. The SU-8 wafer was baked and developed with SU-8 developer, in order to remove the non-cross-linked photoresist.

Calculation of free Gibbs energy ratio of heterogeneous to homogeneous nucleation

According to the Classical Nucleation Theory (CNT), ΔG_{Het} is defined as:

$$\Delta G_{Het} = -\frac{\Delta\mu}{\Omega} V_N + A_{NL}\gamma_{NL} - A_{NS}(\gamma_{SL} - \gamma_{NS}) \quad (1)$$

where $\Delta\mu$ is the chemical potential, Ω is the molar Volume, V_N is the Volume of the nucleus, A_{NL} is the area of the interface between liquid and nucleus, γ_{NL} is the interfacial energy between the nucleus and the liquid, A_{NS} is the interfacial area between the nucleus and the surface, γ_{SL} and γ_{NS} are the interfacial energy between the substrate and the liquid and between the nucleus and the substrate, respectively.

We can define geometrical relations:

$$\alpha = \frac{r}{R} \quad (2)$$

$$\beta = \frac{h}{R} \quad (3)$$

If the topography is applied to a Wenzel's surface [4], where the protein solution is able to follow the geometry filling the cavities, V_N will be given by the sum of the volume of the spherical cap and the volume of the wells on the surface covered by the cap.

$$V_N = \frac{1}{3}\pi R^3[(1-\cos\theta)^2(2+\cos\theta) + \pi R^3 n\alpha^2\beta] \quad (4)$$

A_{NS} (the surface between the nucleus and the surface) will be given by the surface of contact between the nucleus and the surface, including the walls of the wells.

$$A_{NS} = \pi R^2(\sin\theta^2 + 2n\alpha\beta) \quad (5)$$

A_{NL} (the surface between the liquid and the nucleus) will be given by the surface of the spherical cap

$$A_{NL} = 2\pi R^2(1 - \cos\theta) \quad (6)$$

The Young Equation states:

$$\gamma_{SL} - \gamma_{NS} = \gamma_{NL}\cos\theta_Y \quad (7)$$

where θ_Y is the Young's contact angle (contact angle for an ideally flat surface) of the solution on the substrate. When the solution is following the geometry of the surface, θ_Y can be related to the apparent contact angle θ by the Wenzel's equation [5]:

$$\cos\theta_Y = \frac{\cos\theta}{\Gamma} = \frac{\cos\theta\sin\theta^2}{\sin\theta^2 + 2n\alpha\beta} \quad (8)$$

Then, by substitution in equation (1) we obtain:

$$\Delta G_{Het} = -\frac{\Delta\mu}{\Omega}\frac{1}{3}\pi R^3[(1-\cos\theta)^2(2+\cos\theta) + 3n\alpha^2\beta] + \pi\gamma_{SL}R^2[2(1-\cos\theta) - \cos\theta\sin\theta^2] \quad (9)$$

As it is evident from equation (9), ΔG_{Het} is given by a combination of the free energy variation of two events:

1. the formation of a new phase (a spontaneous process that gives a negative contribution to the total variation of free energy, increasing as the volume of the nucleus increases);
2. the formation of a new interface between nucleus and surface and nucleus and liquid (an energetically disfavoured process that has a positive contribution to the total variation of free energy, increasing as the surface of the nucleus increases).

The nucleus size (the radius) determines which of the two energy contributions is prevailing on the total value of Gibbs free energy variation of nucleation. Indeed, small nuclei exhibit high surface to volume ratio, therefore, the interface free energy component has

predominance on the new-phase free energy component causing stabilization of the nuclei by their dissolution. Instead, for nuclei of larger size, the surface of the nuclei is associated with a much larger volume, hence, the new-phase free energy dominates the total free energy determining the stabilization of the nuclei by growth. Therefore, the critical nucleus radius (R*) can be calculated as follows [6]:

$$\frac{\partial \Delta G_{Het}}{\partial R} = 0 \tag{10}$$

$$R^* = \frac{2\gamma_L[2(1-\cos\theta)-\cos\theta\sin\theta^2]}{\left(\frac{\Delta\mu}{\Omega}\right)^2[(1-\cos\theta)^2(2+\cos\theta)+3n\alpha^2\beta]} \tag{11}$$

Replacing R* in Equation (9) we obtain the critical value of Gibbs free energy variation (ΔG_{Het}^*):

$$\Delta G^*_{Het} = \frac{4}{3}\pi\left(\frac{\Delta\mu}{\Omega}\right)^2 {\gamma_L}^3 \frac{[2(1-\cos\theta)-\cos\theta\sin\theta^2]^3}{[(1-\cos\theta)^2(2+\cos\theta)+3n\alpha^2\beta]^2} \tag{12}$$

From CNT we can define the variation of free energy for homogeneous nucleation for the formation of a nucleus of critical size ΔG^*_{Hom} as:

$$\Delta G^*_{Hom} = \frac{16}{3}\pi{\gamma_L}^3\left(\frac{\Delta\mu}{\Omega}\right)^2 \tag{13}$$

Therefore, finally we can obtain $\phi_{117\text{-Nano}}$ as:

$$\Phi_{117-Nano} = \frac{\Delta G^*_{Het}}{\Delta G^*_{Hom}} = \frac{1}{4}\frac{[2(1-\cos\theta)-\cos\theta\sin\theta^2]^3}{[(1-\cos\theta)^2(2+\cos\theta)+3n\alpha^2\beta]^2} \tag{14}$$

In the case of 117-Micro and NR50-Micro the same model (replacing the geometric parameters of a cylinder with the ones of a triangular prism) was applied, for a Wenzel surface.

Therefore, the following geometrical relationships were defined:

$$\alpha_1 = \frac{l}{R} \tag{15}$$

$$\beta_1 = \frac{h_1}{R} \tag{16}$$

Where l is the side of the triangle base of the prisma well and h_1 is the depth.

$$\Phi_{Micro} = \frac{\Delta G^*_{Het}}{\Delta G^*_{Hom}} = \frac{1}{4}\frac{\pi^2[2(1-\cos\theta)-\cos\theta\,\sin\theta^2]^3}{[\pi(1-\cos\theta)^2(2+\cos\theta)+\frac{3}{2}\sqrt{3}n_1{\alpha_1}^2\beta_1]^2} \quad (17)$$

Where n_1 is the number of wells on the contact area between the nucleus and the surface.

For the Hierarchical membrane (Triangular prism wells with cylindrical wells inside), both geometries of the cylinder and prisma were included in the model, resulting:

$$\Phi_{Hierarchical} = \frac{\Delta G^*_{Het}}{\Delta G^*_{Hom}} = \frac{1}{4}\frac{\pi^2[2(1-\cos\theta)-\cos\theta\,\sin\theta^2]^3}{[\pi(1-\cos\theta)^2(2+\cos\theta)+\frac{3}{2}\sqrt{3}n_1{\alpha_1}^2\beta_1+3n\alpha^2\beta]^2} \quad (18)$$

FTIR Analysis on Nafion 117 based membranes

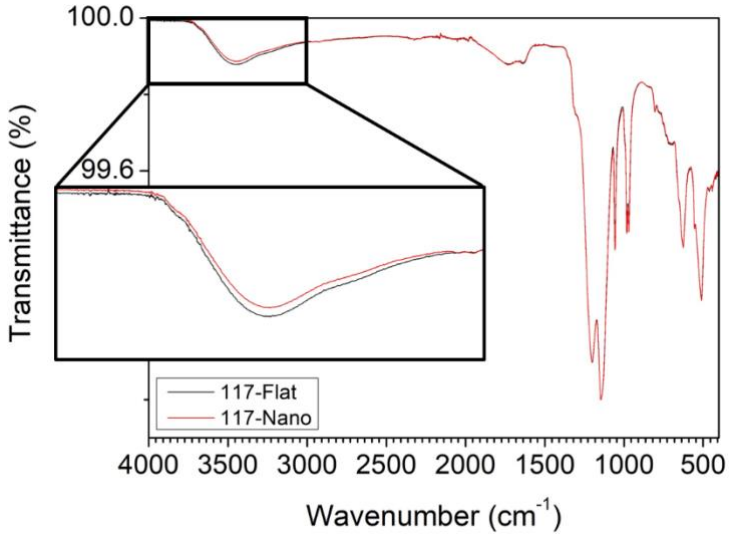

Figure S2. Comparative FTIR analyses of Nafion ®117 based membranes: commercial 117 Flat (reference) and patterned 117 Nano (NIL).

According to the literature, the thermal NIL herein performed would induce minor changes in water content (~2%). In order to confirm such hypotheses, comparative FTIR analyses (see Figure S2) were carried out for as received commercial Nafion® 117 membranes, i.e. sample Flat 117, and for thermal imprinted membranes, i.e. sample 117 Nano. The band centered at 3451 cm^{-1}, attributed to the stretching of –OH group, is only slightly more intense in the case of 117 Flat sample. The remaining part of the two spectra is perfectly overlapping. This observation reinforces the adequacy of the thermal imprinting parameters.

^{19}F19 NMR Analysis on Nafion and NR50 based membranes

The NMR experiments were performed at 376Hz for ^{19}F on a Bruker 400WB Spectrometer. All the spectra were acquired on the sample packed in a 2.5mm rotor with Vespel end-caps, in a 2.5 mm X-H/F double-resonance magic-angle spinning (MAS) probe head at spinning frequencies 20 kHz. The ^{19}F NMR spectra, acquired with a recycle delay of 4 s and a dwell time of 5.6 µs at 20 kHz, are shown below for 117 Flat, 117 Nano and NR50 Flat samples. The spectra were adequately resolved to permit reliable peak assignment and integration

(shown in the upper and lower part of the spectra respectively). The resolved ^{19}F NMR peaks agree quite well with the published data [7]. For all the Nafion based samples, the 19F spectrum is almost identical. It retains signals at -82, -119, which are assigned to side groups CF_3, SCF_2, respectively; and at -123 ppm attributed to some backbone CF_2 groups (denoted as a). The less intense signals at -140 ppm and -146 ppm corresponds to the backbone CF group (denoted as b) and side CF group (denoted as e), respectively.

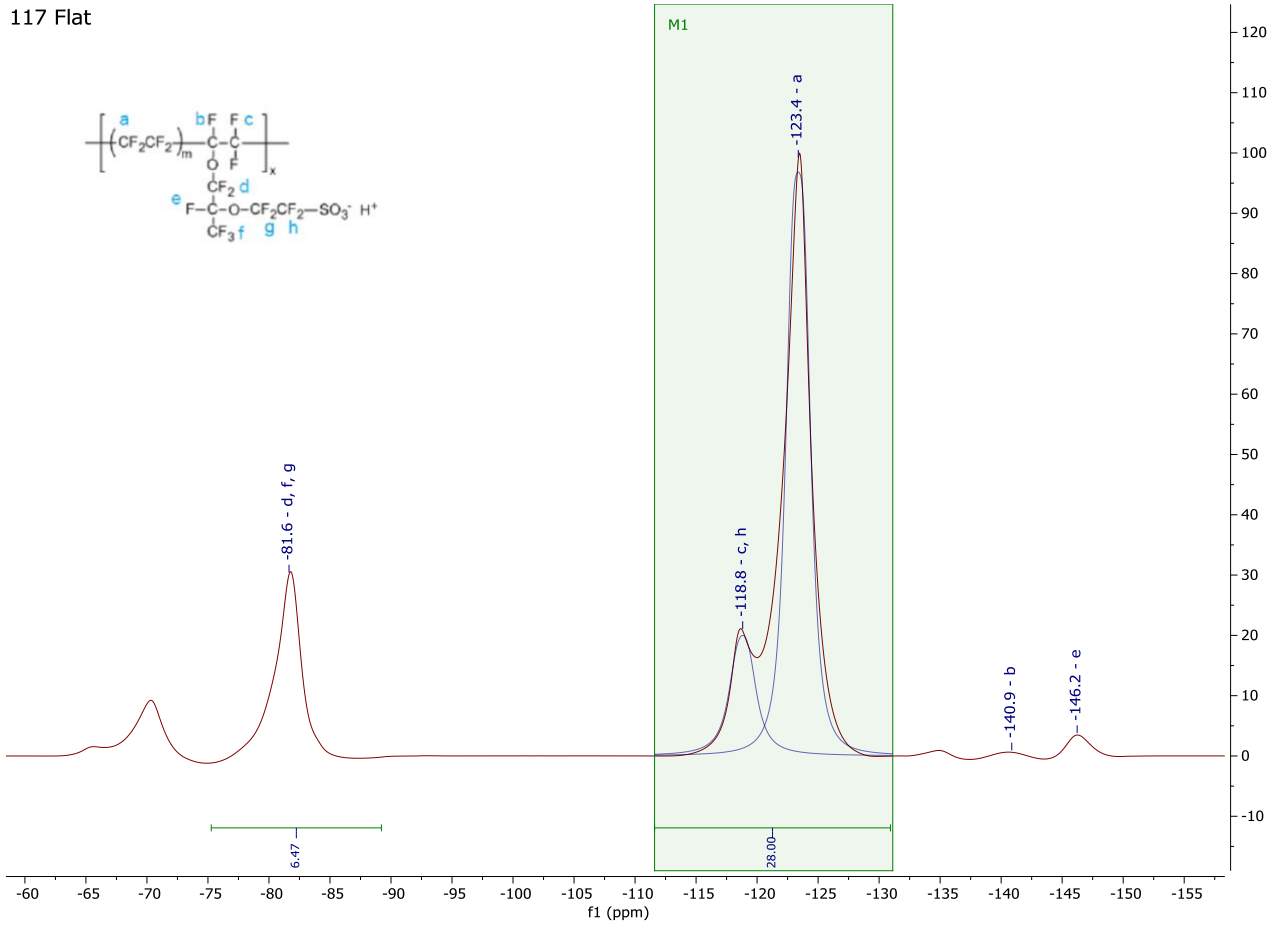

117 Nano

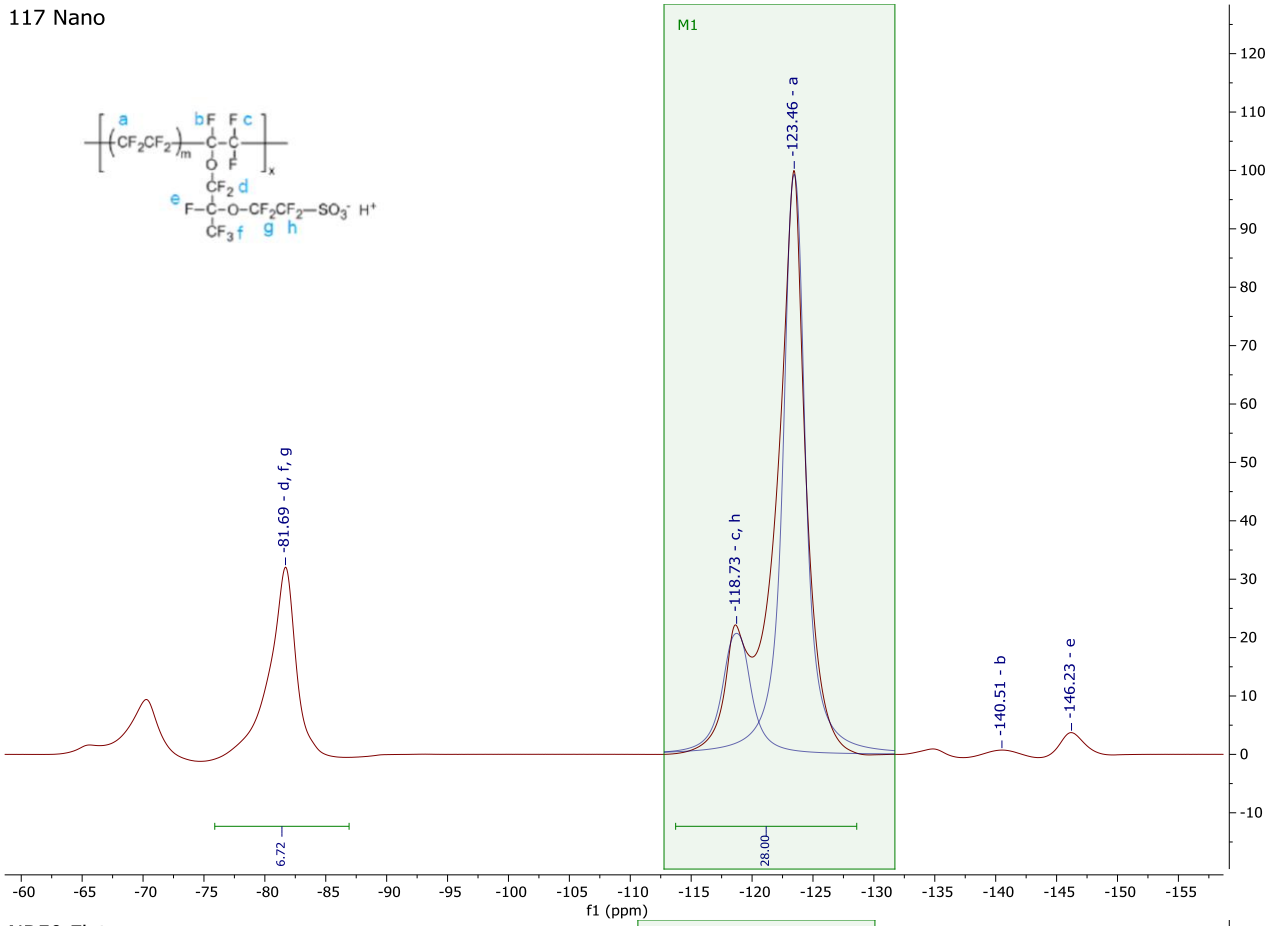

NR50 Flat

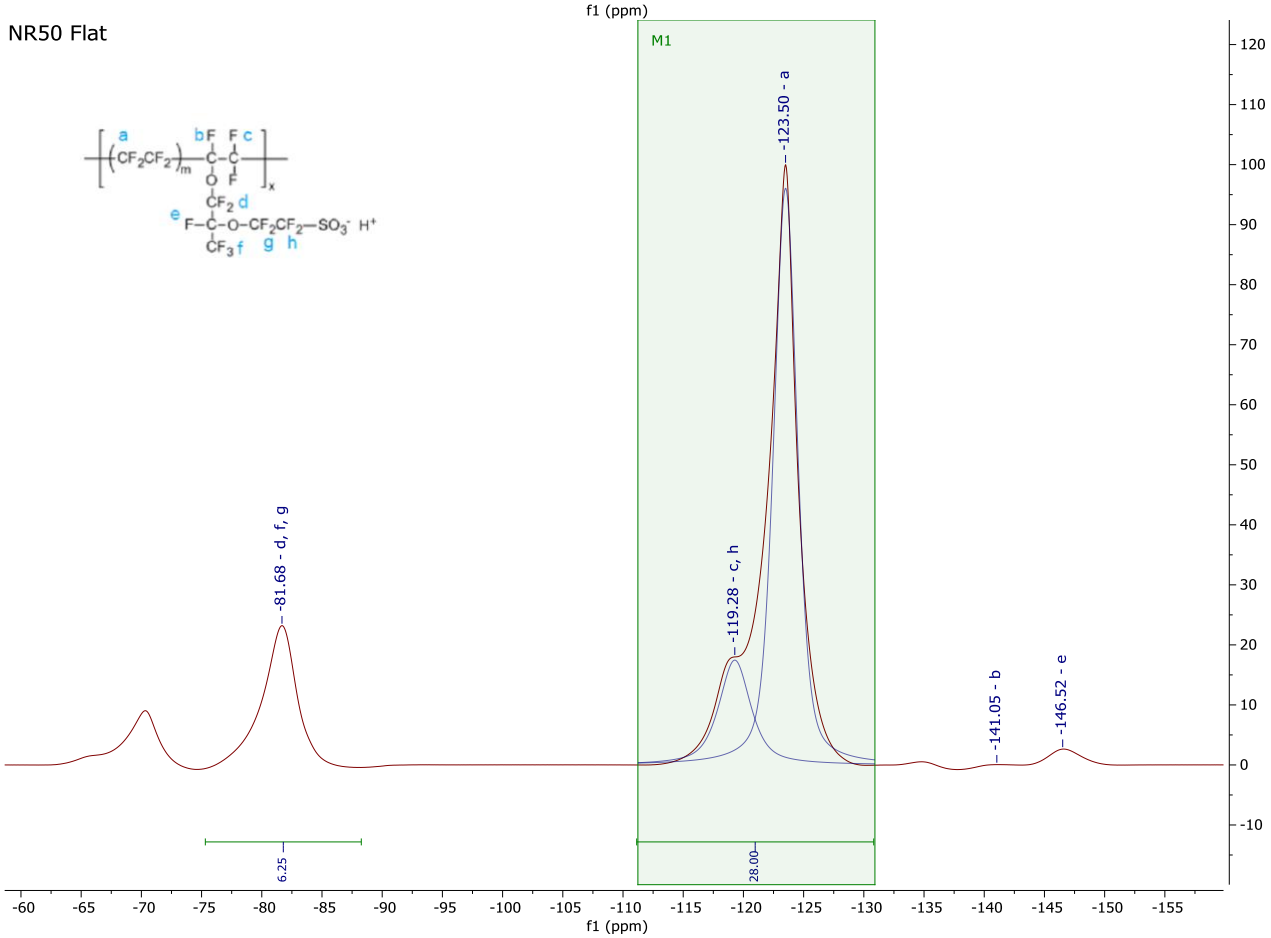

References

[1] S.H. de Almeida, Y. Kawano, Thermal Behavior of Nafion Membrane, J. Therm. Anal. Calorim. 58 (1999) 569–577.

[2] H. Jung, J. Won, Role of the glass transition temperature of Nafion 117 membrane in the preparation of the membrane electrode assembly in a direct methanol fuel cell (DMFC), Int. J. Hydrogen Energy. 37 (2012) 12580–12585.

[3] D. Qin, Y. Xia, G.M. Whitesides, Soft lithography for micro- and nanoscale patterning, Nat. Protoc. 5 (2010) 491–502.

[4] T.S. Meiron, A. Marmur, I.S. Saguy, Contact angle measurement on rough surfaces, Image (Rochester, N.Y.). 274 (2004) 637–644.

[5] E. Celia, T. Darmanin, E.T. De Givenchy, S. Amigoni, F. Guittard, Recent advances in designing superhydrophobic surfaces, J. Colloid Interface Sci. 402 (2013) 1–18.

[6] Y.X. Liu, X.J. Wang, J. Lu, C.B. Ching, Influence of the roughness, topography, and physicochemical properties of chemically modified surfaces on the heterogeneous nucleation of protein crystals, J. Phys. Chem. B. 111 (2007) 13971–13978.

[7] Q. Chen, K. Schmidt-Rohr, 19F and 13C NMR Signal Assignment and Analysis in a Perfluorinated Ionomer (Nafion) by Two-Dimensional Solid-State NMR, Macromolecules 37 (2004) 5995-6003.